PREDICTING OFF-AXIS BONE STRENGTH OF THE DISTAL RADIUS USING HIGH-RESOLUTION PERIPHERAL QUANTITATIVE COMPUTED TOMOGRAPHY BASED FINITE ELEMENT MODELING

A Thesis Submitted to the College of
Graduate and Postdoctoral Studies
in Partial Fulfillment of the Requirements
for the Degree of Master of Science
in the Department of Mechanical Engineering
University of Saskatchewan
Saskatoon

By
AMY TANIA OCTAVIANY BUNYAMIN

PERMISSION TO USE

In presenting this thesis/dissertation in partial fulfillment of the requirements for a Postgraduate degree from the University of Saskatchewan, I agree that the Libraries of this University may make it freely available for inspection. I further agree that permission for copying of this thesis/dissertation in any manner, in whole or in part, for scholarly purposes may be granted by the professor or professors who supervised my thesis/dissertation work or, in their absence, by the Head of the Department or the Dean of the College in which my thesis work was done. It is understood that any copying or publication or use of this thesis/dissertation or parts thereof for financial gain shall not be allowed without my written permission. It is also understood that due recognition shall be given to me and to the University of Saskatchewan in any scholarly use which may be made of any material in my thesis/dissertation.

DISCLAIMER

Reference in this thesis/dissertation to any specific commercial products, process, or service by trade name, trademark, manufacturer, or otherwise, does not constitute or imply its endorsement, recommendation, or favoring by the University of Saskatchewan. The views and opinions of the author expressed herein do not state or reflect those of the University of Saskatchewan, and shall not be used for advertising or product endorsement purposes.

Requests for permission to copy or to make other uses of materials in this thesis/dissertation in whole or part should be addressed to:

Head of the Department of Mechanical Engineering
57 Campus Drive
University of Saskatchewan
Saskatoon, Saskatchewan S7N 5A9 Canada

OR

Dean
College of Graduate and Postdoctoral Studies
University of Saskatchewan
116 Thorvaldson Building, 110 Science Place
Saskatoon, Saskatchewan S7N 5C9 Canada

ABSTRACT

Distal radius fractures are one of the most common types of fractures to occur in older adults. Bone strength (e.g., failure load) of the distal radius can be estimated using finite element (FE) models generated from high-resolution peripheral quantitative computed tomography (HR-pQCT) images; however, these models are limited because they determine failure load under pure compressive loading conditions and neglect off-axis loads that occur during a fall on an outstretched hand. The objective of this research was to identify moment arms in a HR-pQCT distal radius FE model that best predicted off-axis experimental failure load with highest explained variance and least error.

We scanned the distal radius (9.5 mm site) of 21 fresh-frozen cadaveric forearms from female donors (82, SD 9 years) using HR-pQCT. We tested the specimens until fracture in a testing configuration set to simulate a fall on an outstretched hand to obtain experimental failure load. We created FE models which simulated off-axis loading. Specifically, we applied a point load at different medial-dorsal and lateral-dorsal moment arm combinations to determine predicted off-axis failure loads for different failure volumes and different failure criterion. We report the moment arm combination with the highest explained variance (R^2) and lowest root mean squared error (RMSE%) in experimental failure loads.

When incorporating off-axis loading, applying a 1 mm dorsal moment arm explained up to 79% of variance in experimental failure load, improving explained variance from pure compressive loading by 4%. These findings suggest that accounting for off-axis loading in current HR-pQCT FE models appear to offer modest improvement to the prediction of distal radius failure load which may potentially help to improve identification of individuals at risk of wrist fracture, and prevention and treatment therapies.

ACKNOWLEDGEMENTS

I would like to give my sincere gratitude and thanks for everyone who have made the completion of this thesis possible. Foremost, I would like to thank my supervisors, Dr. J.D. Johnston and Dr. Saija Kontulainen, for their guidance and patience throughout my program as well as my time as a summer student. Their mentorship and insight were invaluable throughout the entire process and I cannot thank them enough.

I would also like to thank my committee members, Dr. Allan Dolovich, Dr. Catherine Trask, and Dr. Akindele Odeshi, for their contribution and assistance in this research.

I would also like to acknowledge the current and former members of our research group: Kadin, Kirstin, Dylan, Alvaro, Pablo, Lumeng, Dena, Ibk, Josje, Nima, Mahdi, Mehrdad, Dustin, Tim, and Brennan. Thank you all for your insight and support with this research. I will always cherish the time we shared together in our zany, little office and I wish you all the best in wherever life takes you.

I would also like to thank my family and friends for their love, encouragement, and unwavering support throughout my studies. I could not have done this without you.

Finally, I would like to thank the Natural Sciences and Engineering Research Council (NSERC; CGS-M, USRA, Discovery Grant) and the University of Saskatchewan (Dean's Scholarship) for financial support.

TABLE OF CONTENTS

LIST OF TABLES

LIST OF FIGURES

LIST OF TERMS, ABBREVIATIONS, AND SYMBOLS

TERM	DEFINITION
Anisotropic material	A material with mechanical properties that are direction-dependent
Anterior	Situated closer to the front of the body
Apparent modulus	Ratio of apparent stress and apparent strain within the elastic range
Apparent strain	Change in length over the original length of the whole bone model
Apparent stress	Reaction force over the projected cross-sectional bone area
Axial	Oriented along the longitudinal axis of the body
Distal	Situated away from the center of the body
Dorsal	Located near the back (posterior of hand) in transverse plane
Ex vivo	An experiment taking place outside a living organism
In vivo	An experiment taking place inside a living organism
Isotropic material	A material with identical mechanical properties in different directions
Isotropic voxel	Voxel with the same dimensions in all directions
Lateral	Situated closer to the side of the body in the frontal plane
Medial	Situated closer to the middle of the body in the frontal plane
Moment	Product of an applied force and the distance to the object from a reference point (i.e., moment arm)
Poisson's ratio	Ratio of transverse to longitudinal strains
Posterior	Situated closer to the back of the body in the transverse plane
Principal stress	Normal stresses (i.e., stress acting perpendicular to surface) where the shear stress is zero
Shear stress	Stress due to force acting parallel to the bone surface
Stiffness	The extent to which an object resists deformation
Strain	Ratio of change in length to the original length
Stress	Force acting on an area divided by the area

ABBREVIATION	DEFINITION
2D	Two-dimensional
3D	Three-dimensional
aBMD	Areal bone mineral density
BCM	Brittle Coulomb Mohr
BMD	Bone mineral density
BMC	Bone mineral content
CT	Computed tomography
DXA	Dual-energy x-ray absorptiometry
FE	Finite element
HA	Hydroxyapatite
HR-pQCT	High-resolution peripheral quantitative computed tomography
IPL	Image Processing Language
PMMA	Polymethylmethacrylate
pQCT	Peripheral quantitative computed tomography
R^2	Coefficient of determination
RMSE%	Root mean squared error percentage
ROI	Region of interest
SD	Standard deviation
STM	Single tissue model
VOI	Volume of interest
WHO	World Health Organization

SYMBOL	DEFINITION
2D	Two-dimensional
3D	Three-dimensional
E	Elastic modulus [MPa]
F	Force
F_x	Force acting along the x-axis direction [N]
F_y	Force acting along the y-axis direction [N]
F_z	Force acting along the z-axis direction [N]
GPa	Gigapascals
kV	Kilovolts
mA	Milliamps
mg	Milligram
mm	Millimeter
ms	Microsecond
µm	Micrometer
MPa	Megapascals
M	Moment
N	Newtons
P	Applied load or force
Sv	Sievert (unit of ionizing radiation dose)
U	Strain energy density [MPa]
ε	Strain
ε_{yt}	Tensile yield strain
ε_{yc}	Compressive strain
ε_{eff}	Effective strain
ε_{vm}	von Mises strain
ε_1	Biggest principal strain
ε_2	Median principal strain
ε_3	Smallest principal strain
σ	Stress [MPa]

$\bar{x}$	Moment arm in the x-direction
$\bar{y}$	Moment arm in the y-direction

1 INTRODUCTION

1.1 Overview

Osteoporosis is a disease characterized by low bone mass and deterioration of bone micro-architecture [1]. Distal radius fractures are one of the most common types of osteoporotic fracture to occur in older adults [2,3]. A distal radius (or wrist) fracture, typically due to a fall on an outstretched hand from standing height or less, occurs when the external forces applied to bone exceeds bone strength (i.e., failure load).

Since individuals who have experienced a distal radius fracture may be at risk for future osteoporotic fractures (e.g., hip, spine or wrist fractures) [4,5], it may be beneficial to assess distal radius strength in order to provide early indication of an individual's risk of future osteoporotic fractures. This can be done using a variety of different imaging modalities, including high-resolution peripheral quantitative computed tomography (HR-pQCT). HR-pQCT allows for three-dimensional (3D) imaging of bone micro-architecture and bone density and, when combined with computational finite element (FE) analysis, is an attractive, non-invasive tool to quantify distal radius bone strength *in vivo* [6]. An FE model of a segment of bone taken at the distal radius is created from the HR-pQCT images by directly converting bone tissue voxels to equally-sized hexahedral brick elements while ignoring bone marrow (i.e., models consists of two materials – bone and air). These models are generally linear and boundary conditions typically simulate uniaxial compression on the distal radius section, where failure is defined when a percentage of elements exceed a specified criterion (e.g., strain or stress limit).

Current HR-pQCT FE models that simulate uniaxial or pure compression explain 75% variance in experimental failure load. These models assume that failure occurs when 2% of all elements exceed an energy-equivalent strain limit of 7000 μstrain [7]. It may be possible to improve explained variance by accounting for off-axis loads as well as considering other failure criterion and different percentages and volumes of failed tissue. Previous findings, based on a simulation done on a single participant, suggest that accounting for off-axis loading in radius models may be beneficial as off-axis failure loads were up to 47% lower than their respective axial failure loads [8].

Thus, the overall aim of this thesis was to account for off-axis loading in HR-pQCT FE models and identify moment arms in a HR-pQCT distal radius FE model that best predicted off-axis experimental failure load with highest explained variance and least error.

1.2 Scope

Chapter 2 of this thesis discusses current literature, wrist anatomy and bone composition, medical imaging techniques, mechanical testing, and FE analyses. The research question and objective are defined in Chapter 3. Chapter 4 outlines the methodology used for sample preparation, mechanical testing, imaging and FE modeling. I discuss the results obtained from this study in Chapter 5. Limitations and potential future work are outlined in Chapter 6.

2 LITERATURE REVIEW

2.1 Anatomy

2.1.1 Wrist Structure

The wrist consists of the distal radius and ulna, proximal carpal bones (i.e., scaphoid, lunate, triquetrum), the radiocarpal joint, and the distal radioulnar joint (Figure 2-1) [9]. The radiocarpal joint allows for flexion and extension of the wrist. The distal radioulnar joint allows for pronation and supination of the forearm. The primary area of interest for this study is the radius, as distal radius fractures are common in older adults, primarily postmenopausal women [2,4].

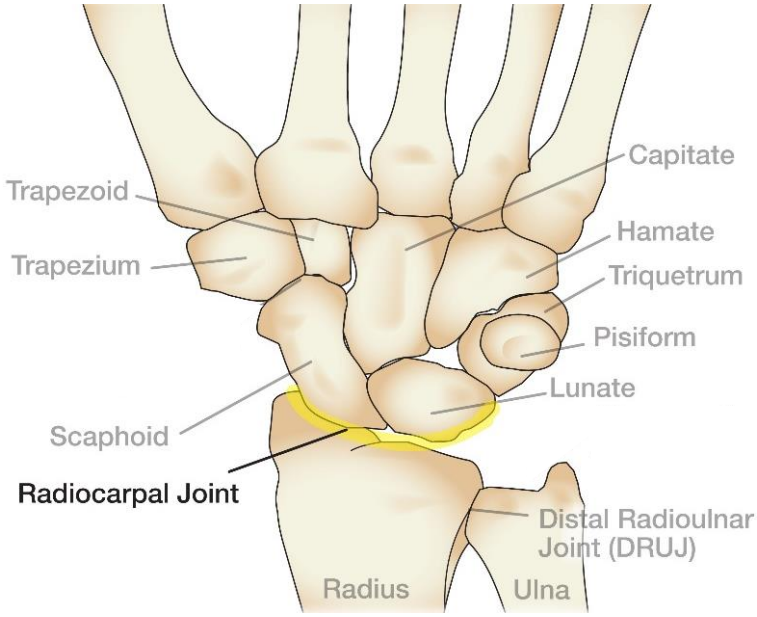

Figure 2-1. Diagram of distal forearm bones in the left hand, carpal bones, radiocarpal joint, and distal radioulnar joint. *Modified from the American Society for Surgery of the Hand.*

The radius, which is one type of long bone in the appendicular skeleton, consists of 3 regions: the diaphysis, metaphysis, and epiphysis. The majority of osteoporotic distal radius fractures occur within the metaphysis, where the radial diaphysis or shaft widens to create the rectangular end of the distal radius or the epiphyseal region (Figure 2-2A). This rectangular end has two articular surfaces to allow for movement or articulation between the radius and ulna (ulnar notch) as well as the radius and the scaphoid and lunate (scaphoid and lunate facets, respectively). Also, on the lateral side of the distal radius there is the styloid process, which works as an attachment point for muscles and ligaments. The palmar surface of the distal radius has a thick ridge, allowing for connection to the palmar radiocarpal ligament of the wrist joint. On the dorsal

surface there is the Lister's tubercle, which provides an attachment point for the dorsal radiocarpal ligament and is traversed by tendons (Figure 2-2B).

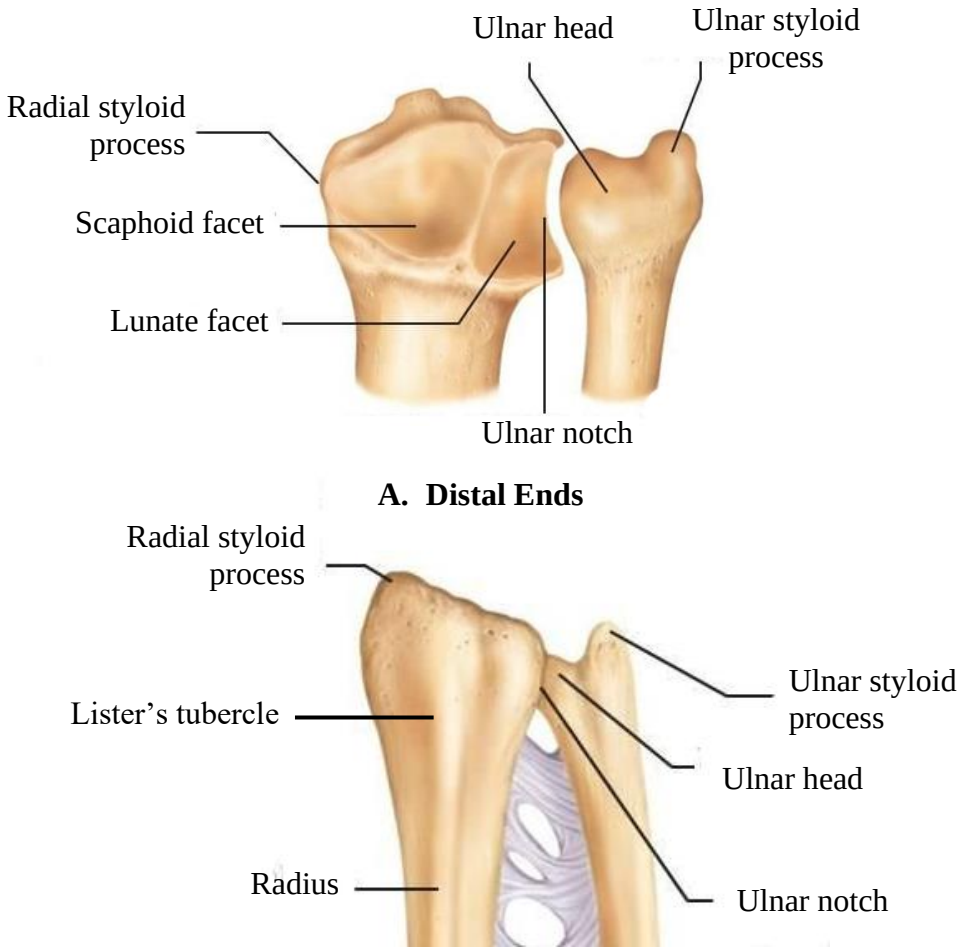

Figure 2-2. A) Distal ends of the radius and ulna in the right hand, illustrating radial and ulna styloid process, ulnar head, ulnar notch, and the scaphoid and lunate facets; B) Posterior view of the distal ends of the radius and ulna in the right hand. *Modified from Marieb (2004)* [10].

2.1.2 Bony Composition

At a macroscopic level, the radius consists of two types of bone tissue: cortical and trabecular bone (Figure 2-3). Cortical bone is a dense bone that has some level of porosity. The amount of porosity in cortical bone can affect the overall strength of the cortical shell [11,12]. This is important because cortical bone is the main load-bearing structure in the distal radius and cortical bone properties (e.g., porosity, thickness, density) are contributors to overall strength of the whole bone [13]. Cortical bone surrounds trabecular bone, which has a more porous composition, with large spaces

between the bony lattice-like network of plates and rods [9]. Trabecular bone is organized to optimize load transfer from the articular surface of the distal radius to the load-bearing cortical bone [14]. Within the distal radius (i.e., the epiphyseal and metaphyseal region), the bone consists primarily of weaker trabecular bone and thin cortical shell, predisposing this area to fractures.

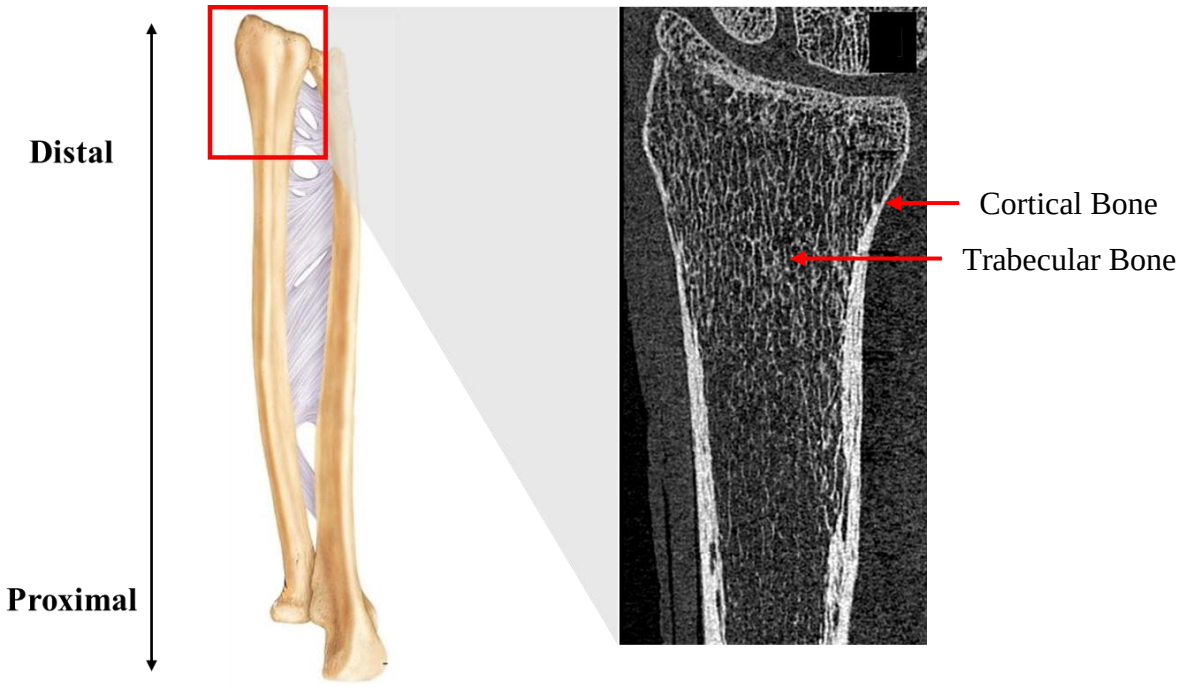

Figure 2-3. Anatomy of the long bones in the right forearm. Left: Diagram of the radius indicating the distal and proximal locations. Right: High-resolution peripheral quantitative computed tomography (HR-pQCT) scan of the distal radius with the cortical and trabecular bone identified. *Modified from Martini et al. (2012) [9] and van Lenthe and Muller (2008) [15].*

2.2 Distal Radius Fractures

Distal radius fractures occur when the load applied to the radius (e.g., load due to a fall on an outstretched hand) exceeds the bone's failure load. The likelihood of a fracture occurring is determined by an individual's risk of fracture. Globally, there have been 1.7 million distal radius fractures reported in older adults (i.e., adults older than 50 years), with distal radius fractures most commonly reported in adults ranging between 50-65 years and postmenopausal women [2,3].

2.2.1 Osteoporotic Fractures

Osteoporosis is a disease characterized by low bone mass and deterioration of bone micro-architecture [1]. This disease affects 200 million people worldwide and the incidence of osteoporotic related fractures (e.g., distal radius fractures) are projected to increase by approximately 50% by 2025 due to an aging population [16,17]. Distal radius fractures are one of

the most common types of osteoporotic fractures in older adults, accounting for 1.7 million annual fractures worldwide [2,3]. Distal radius fractures may be an early indicator of a weakened skeleton and future osteoporotic fractures [18]; thus, it may be beneficial to identify individuals who are prone to forearm fractures to implement appropriate prevention strategies (e.g., drug therapy, targeted exercises).

2.2.2 Loading of the Radius

During a fall, the radius will experience a combination of compression, bending moments, and shear (Figure 2-4) [19,20]. The axial, compressive force is primarily due to the applied load experienced during the fall; however, the radius will also experience some contact force from the scaphoid. Bending in the radius is due to the combined effect of two bending moments. The first bending moment is due to the dorsally-directed force and the second bending moment is due to the palmar and collateral ligaments limiting hyper-dorsiflexion (i.e., hyper-extension) of the hand during a fall (M_{Fy} and $M_{ligaments}$, respectively, in Figure 2-4C). The radius also experiences shear due to the dorsally directed load.

In the case of a fall, 15% of fracture cases were due to an axial load applied to the radius [21]. This small proportion is important as most studies only consider axial loading when predicting distal radius failure load [6,22-25]. Troy and Grabiner's findings suggest that accounting for off-axis loading may be beneficial as they found that off-axis strength outcomes (e.g., failure load, ultimate stress) were up to 47% lower than their respective axial outcomes [8]; however, their findings were based on a single participant. To account for off-axis loading, Troy et al. recommend applying an axial load at an offset of 8 mm medial and 7 mm dorsal from the centroid [26]. This recommendation, however, was based on a two-dimensional (2D) model generated from a cross-sectional peripheral quantitative computed tomography (pQCT) scan of the distal radius with a small sample size (n=3). It is unknown if it is applicable to 3D models of the distal radius taken from a different imaging modality.

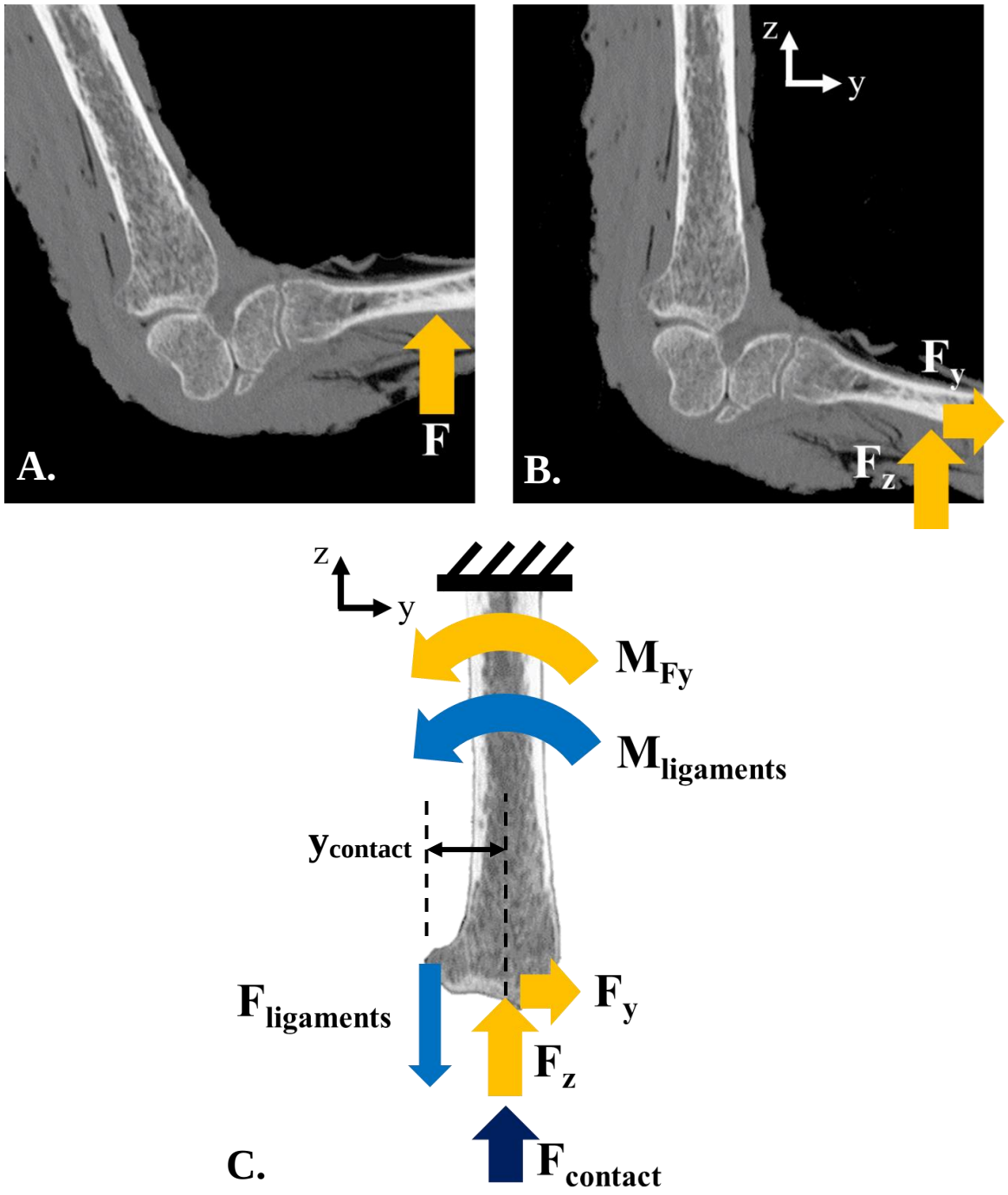

Figure 2-4. A) Falling load (*F*) experienced by an outstretched hand during a fall; B) Hand realigned to y-z axes, and the falling load is broken into it's y-component (i.e., dorsal), F_y, and z-component (i.e., axial), F_z; C) Loading experienced by the radius during a fall on an outstretched hand. Axial loads applied to the radius are due to the falling load (F_z), contact between the radius and scaphoid ($F_{contact}$), and tensile loads generated in the ligaments ($F_{ligaments}$). Bending moments in the radius are due to F_y (M_{Fy}) and $F_{ligaments}$ when restricting hyper-dorsiflexion (i.e., hyper-extension) of the hand during a fall ($M_{ligaments}$). $M_{ligaments}$ is generated by multiplying $F_{ligaments}$ by the moment arm, $y_{contact}$, which is the distance to the contact region between the scaphoid and radius and $F_{ligaments}$. The radius also experiences shear due to the dorsally directed load, F_y. *Modified from McDonald (2017)* [(27)].

2.2.3 Estimation of Fracture Risk

2.2.3.1 Dual-energy X-ray Absorptiometry (DXA)

Dual-energy x-ray absorptiometry (DXA) is a commonly used bone densitometry method for diagnosing osteoporosis [28]. DXA, through radiographic absorption techniques, obtains 2D projections of the amount of bone present in a projected area (i.e., bone mineral content or BMC). By dividing BMC by the projected area, areal bone mineral density (aBMD, mg/cm^2) can be obtained. According to the World Health Organization (WHO), osteoporosis is clinically defined as an aBMD value (obtained from either the femoral neck or spine) that lies 2.5 standard deviations or more below the average value for a healthy 30-year-old woman (i.e., T-score $\leq$ -2.5).

Since a 2D projection is used to represent a 3D structure, DXA aBMD measures are size-dependent, as larger individuals will have more bone mineral within the projected area. Although BMC and aBMD measures have been validated at the distal radius (BMC: R^2=0.53; aBMD: R^2=0.60) [29,30], aBMD may not be the best indicator of failure load because DXA is unable to account for variations in bone microstructure (e.g., cortical thickness, cortical porosity, trabecular number) that are determinants of failure load [31].

2.2.3.2 Peripheral Quantitative Computed Tomography (pQCT) and High-resolution pQCT

Three-dimensional measures of bone density and bone microstructure can be obtained from peripheral quantitative computed tomography (pQCT) and high-resolution pQCT (HR-pQCT) imaging. These imaging modalities can measure distal and shaft (pQCT only) sites of the radius and tibia, with resolutions that are adequate for *in-vivo* characterization of cortical and trabecular micro-architecture (82-400 µm) [32,33]. pQCT based total BMC measures have been validated at the distal radius (R^2=0.66-0.79) [30,34,35].

Currently, HR-pQCT images are acquired using either the 1st or 2nd generation XtremeCT device (XtremeCT, Scanco Medical AG, Brüttsellen, Switzerland). The 1st generation uses the following scan settings for *in vivo* imaging: 82 µm voxel size, 60 kV voltage, 1 mA current, and 200 ms integration time. According to the recommended manufacturer settings, a 9.02 mm area of the distal radius is obtained by acquiring 110 parallel slices, located 9.5 mm proximal to the mid-region of the radial endplate (Figure 2-5) [36]. The 2nd generation (i.e., XtremeCT II) can image bone using a voxel size of 61 µm with shorter scan times (2.0 vs. 2.8 min) and slightly higher radiation dose (<5 vs. <3 µSv) (Figure 2-6) [37]. The LIMBS lab in the University of Saskatchewan College of Kinesiology is equipped with the 1st generation XtremeCT.

HR-pQCT, in conjunction with FE modeling, can also provide estimates of bone strength, specifically failure load, ultimate stress at failure, stiffness, and apparent modulus [38-48]. FE models incorporate information pertaining to both structural and material bone properties, which are not considered when looking only at structural (e.g., area, area moment of inertia) or density measures. This can be beneficial as a recent prospective study found that HR-pQCT FE failure load was the strongest predictor of incident fracture risk at the radius and tibia in older adults [49].

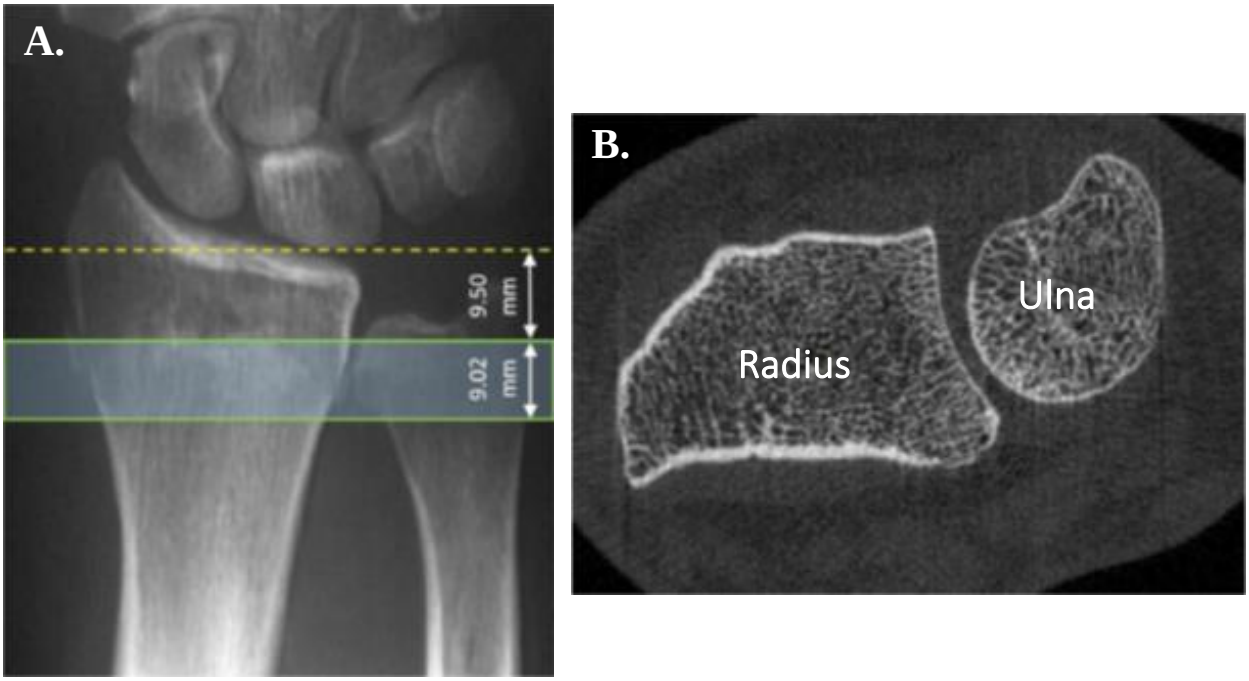

Figure 2-5. (a) Location of the scanned standard (clinical) region of the distal radius. The reference line (i.e., mid-region of the radial endplate) is indicated by the dotted yellow line. The scanned region is represented by the green rectangle. (b) Cross-sectional view of a HR-pQCT scan of the left wrist [(36)].

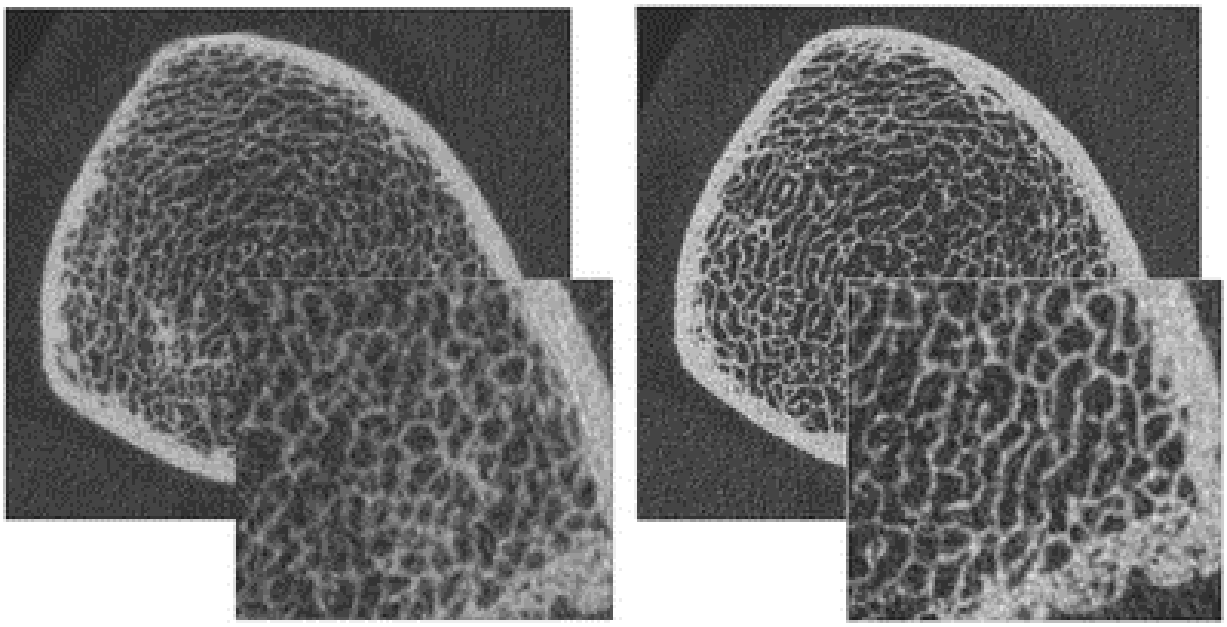

XtremeCT I (82 µm) **XtremeCT II (61 µm)**

Figure 2-6. Image of the same tibial cross-sectional slice obtained from the 1st generation XtremeCT (XtremeCT I) at a voxel size of 82 µm (*left*) and the 2nd generation XtremeCT (XtremeCT II) at 61 µm (*right*). *Modified from Agarwal et al. (2016)* [(37)].

2.3 Measuring Bone Strength

Mechanical testing is the gold standard of measuring bone strength. In this area of research, mechanical tests are typically used to develop predictive models by quantifying bone strength and correlating image-derived metrics to the quantified outcome. There are three types of mechanical tests of the distal radius:

1. Testing of segments or pucks of bone obtained from the distal radius
2. Testing of the excised radius
3. Testing of the intact hand and forearm

2.3.1 Testing of Distal Radius Segments

When testing segments of the distal radius, the bone segment is exposed to a pure compressive load until failure (Figure 2-7). Predicted distal radius failure loads, acquired using linear FE models, have been validated against failure loads acquired via mechanical testing of cadaveric distal radius segments. High correlations (R^2=0.94-99% [23,50,51]) obtained using this method were likely due to the exact match between the bone segment and the scanned region utilized in the FE analysis. This method, however, does not reproduce a distal radius fracture during a fall on an outstretched hand and is instead a representation of the strength of the local region where the image was obtained.

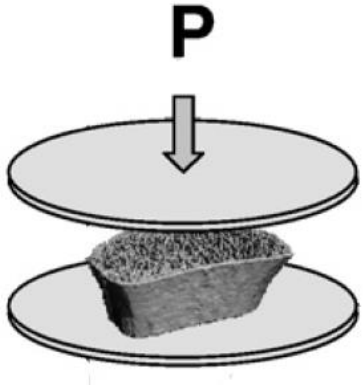

Figure 2-7. Uniaxial compression performed on distal radius segment. *Modified from MacNeil and Boyd (2008) [23].*

2.3.2 Testing of Excised Radii

Some of the limitations associated with mechanical tests of distal radius segments can be negated by using tests of the excised radius. When using excised radii, linear HR-pQCT FE models can explain 92% variance in experimental failure load [24]; however, this method is also limited when reproducing a distal radius fracture during a fall on an outstretched hand due to the absence of soft

tissues. By removing the soft tissues, it is difficult to apply a bending moment to the distal radius that is needed to reproduce a distal radius fracture [19]. To overcome this, excised radius testing protocols include embedding both ends of the radius and aligning the bone at 15° in order to simulate bending that would occur during a fall (Figure 2-8). However, by constraining both ends of the radius, Wagner et al. found that the internal loads experience by the excised radius were primarily compressive in nature [19]

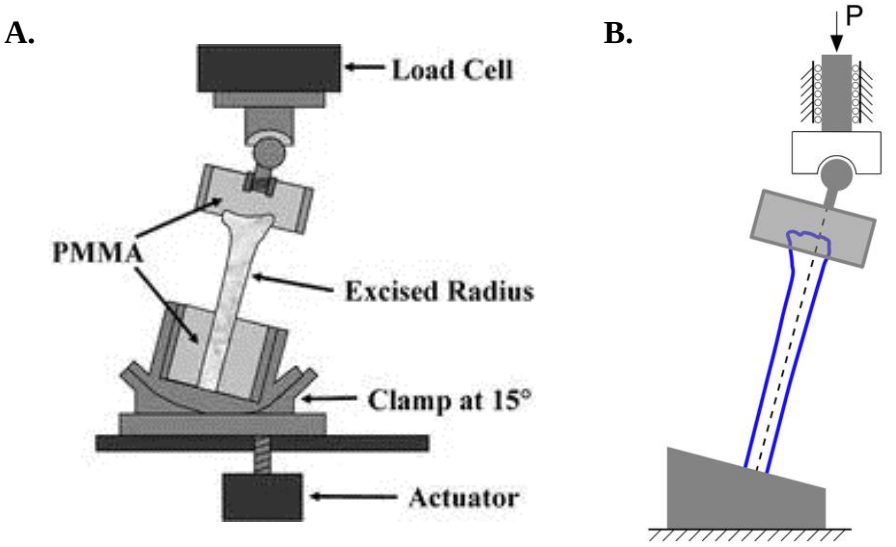

Figure 2-8. (a) Excised radius mechanical testing configuration and (b) representative loading of testing protocol. *Image from Muller et al. (2003) [30] and Wagner et al. (2012) [19].*

2.3.3 Testing of Intact Forearms

The use of intact specimens in mechanical tests allows for a more representative scenario of a distal radius fracture due to a fall on an outstretched hand as it incorporates the effect of other tissues (e.g., ligaments), joints, and surrounding bones. It is difficult to quantify the exact force directions and magnitudes experienced by the radius when testing intact forearms [34]; however, studies that have utilized intact forearms were successful in reproducing distal radius fractures with explained variance in experimental failure load ranging between 66% to 75% [22,25,52]. Intact forearm testing protocols include positioning the forearm in 15° dorsal inclination from the vertical in order to replicate the impact posture during a fall on an outstretched hand and loading the forearm via a vertically applied force on the dorsiflexed palm (Figure 2-9) [19]. This loading protocol allows the hand to continuously flex throughout the mechanical test, replicating the loading that would occur during a fall onto an outstretched hand.

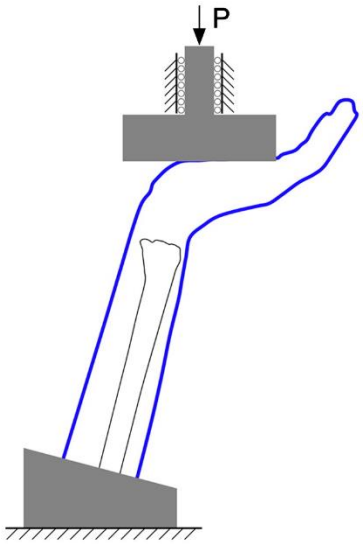

Figure 2-9. Representative loading of the intact forearm testing protocol. *Image from Wagner et al. (2012)* [19].

2.3.4 Effects of Embalming

Mechanical testing outcomes can be affected by the storage method used. Fixation or embalming of cadaveric specimens can alter the mechanical properties of bone (e.g., ultimate strength, modulus of elasticity, hardness), primarily due to the prolonged exposure to formalin [53-56]. This variation in mechanical properties can be negated when using fresh-frozen cadaveric specimens; thus, it is preferential to use fresh-frozen cadaveric specimens in order to have a closer representation of *in vivo* conditions.

2.3.5 Load-Displacement Curve

Experimental mechanical tests are conducted by applying either a varying load or displacement against the specimen. From this, a load-displacement curve can be created from the change in load or displacement with time (Figure 2-10). The slope of the linear region of the curve corresponds to the stiffness of bone, the peak of the curve corresponds to the failure load, and the area under the curve is the energy until failure.

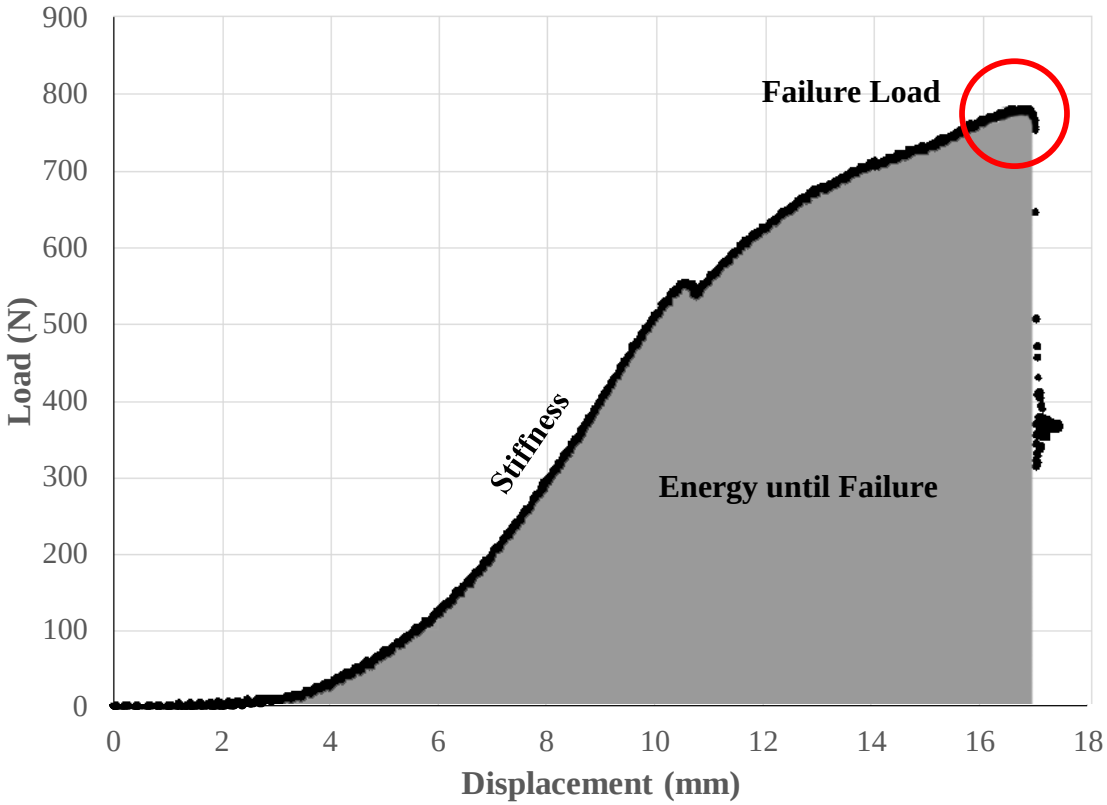

Figure 2-10. Load-displacement curve. The slope of the linear region corresponds to the stiffness of bone and the peak load corresponds to the failure load. The area under the curve is the energy until failure.

2.4 Finite Element (FE) Modeling

FE modeling is a numerical technique used to obtain solutions to differential equations that describe a complicated mechanical problem (e.g., complex structure, such as bone). This is achieved by dividing the object into a number of small finite elements of a simple geometry so the deformation and stresses can be easily calculated [57]. Subject-specific FE models typically use CT images to define bone geometry and assign material properties and, with sufficient resolution, are able to incorporate variations in both bone architecture and mechanical properties [6,23,52,57].

2.4.1 Discrete vs. Continuum FE

Subject-specific FE models can be described as either *discrete* or *continuum* models. In discrete FE models, the bone microstructure is directly imaged and modeled. This model is the standard approach in HR-pQCT, where bone is assigned an elastic modulus of 6.829 or 10 GPa [23,52]. If the bone microstructure cannot be directly imaged (e.g., clinical CT images), a continuum FE model

can be used. With this approach, elastic moduli are estimated based on local BMD using published density-modulus relationships derived from experimental data (e.g., $E = 10(BMD)^2$).

To date, there are two discrete and one continuum HR-pQCT FE model reported in the literature. The discrete models include: 1) homogenous single-tissue model (i.e., STM), where the same material properties are assigned to cortical and trabecular bone [22,52]; and 2) homogenous dual-tissues model (i.e., DTM), where different material properties are assigned to cortical and trabecular bone [58]. The continuum-based model defines heterogenous material properties using the density-modulus equation shown below (Equation 2.1) [23]. In general, for the distal radius, the discrete models both converge in ~3 hours and the continuum model converges in ~5 hours [59].

$$E = 15\left(\frac{\mathrm{BMD}}{1200}\right)^{1.7} \quad (2.1)$$

2.4.2 Failure Criteria

When conducting FE analyses, some considerations must be made, such as the modeling approach (i.e., linear vs. non-linear model) and the failure criterion utilized in the model. A failure criterion is a set of equations and conditions that must be met in order to define failure of the model. It is currently unknown which failure criterion should be utilized with HR-pQCT FE models which simulate off-axis loading. In this study, we will focus on the following strain-based failure criterion (Table 2-1) [60]:

1) Energy-Equivalent Effective Strain [52]
2) Hoffman Strain [61]
3) Maximum Principal Strain [62]
4) von Mises Strain [62]

Table 2-1. Summary of failure criterion investigated in study and their respective equations

Failure Criterion	**Equation(s)**
Energy-Equivalent Effective Strain (ε_{eff})	$\frac{\varepsilon_{yc}}{\varepsilon_{eff}} \leq 1$ Where, $\varepsilon_{eff} = \sqrt{\frac{2U}{E}}$ and $U = \frac{1}{2}(\sigma_1\varepsilon_1 + \sigma_2\varepsilon_2 + \sigma_3\varepsilon_3)$
Hoffman Strain (ε_{hoff})	$\frac{1}{2\varepsilon_{yt}\varepsilon_{yc}}[(\varepsilon_1 - \varepsilon_2)^2 + (\varepsilon_1 - \varepsilon_3)^2 + (\varepsilon_2 - \varepsilon_3)^2] + \left(\frac{1}{\varepsilon_{yt}} - \frac{1}{\varepsilon_{yc}}\right)(\varepsilon_1 + \varepsilon_2 + \varepsilon_3) \geq 1$
Maximum Principal Strain (ε_{max})	$\frac{\varepsilon_{yt}}{\varepsilon_1} \leq 1$ or $\frac{\varepsilon_{yc}}{\varepsilon_3} \geq -1$
von Mises Equivalent Strain (ε_{vm})	$\frac{\varepsilon_{yc}}{\varepsilon_{vm}} \leq 1$ Where, $\varepsilon_{vm} = \sqrt{\frac{1}{2}[(\varepsilon_1 - \varepsilon_2)^2 + (\varepsilon_1 - \varepsilon_3)^2 + (\varepsilon_2 - \varepsilon_3)^2]}$

2.4.2.1 Linear vs. Non-Linear

Linear FE models assume that the load-displacement curve has a linear relation; however, this model does not account for nonlinear effects caused by deformation of the bone micro-architecture. Non-linear models can predict bone strength properties directly and can estimate post-yield behavior of bone [23,63,64]; however, these models can be time-consuming and computationally demanding, taking approximately 10 times longer to complete than linear models [23], limiting their feasibility for clinical use. Also, others have observed only small improvements in bone strength properties (e.g., ultimate failure stress) when using non-linear models under pure compression [23]. An example of a non-linear bone material model is shown in Figure 2-11.

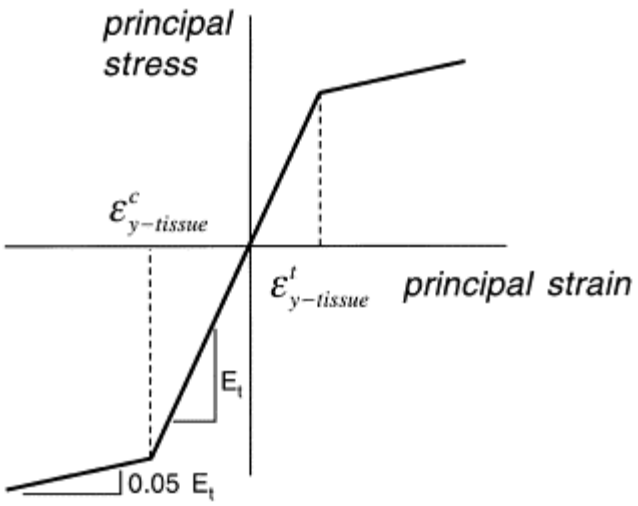

Figure 2-11. Bilinear constitutive model for trabecular bone, assuming the elastic constants of the tissue decreased isotropically when the principal strains exceed their tensile (ε_y^t) or compressive (ε_y^c) tissue yield strain. *Image from Niebur et al. (2000)* [63]

2.4.2.2 Energy-Equivalent Effective Strain

Effective strain failure criterion was first introduced by Pistoia et al. where an energy-equivalent strain (i.e., effective strain) was introduced based on non-linear FE studies [52]. According to this criterion, the bone model had failed when 2% of all elements had values that exceed a tissue effective strain of 7000 μstrain. This effective strain value can be calculated using the following equation, where ε_{eff} is the effective strain, U is the strain energy density [MPa], and E is the elastic modulus [MPa].

$$\varepsilon_{eff} = \sqrt{\frac{2U}{E}} \tag{2.2}$$

It is unknown how changing the percentage of failed tissue (e.g., varying from 2%) will affect predictions of off-axis HR-pQCT failure load. To our knowledge, only Mueller et al. [25] investigated the effect of different percentages of failed tissue on predicted failure loads; however, they simulated pure compressive loading conditions and used embalmed specimens, which can alter the mechanical properties of bone [65].

2.4.2.3 Hoffman Strain

The Hoffman Strain failure criterion was initially developed to determine failure of brittle composite materials [61]. This failure criterion, for linear isotropic materials, is defined by the following equation.

$$\frac{1}{2\varepsilon_{yt}\varepsilon_{yc}}[(\varepsilon_1-\varepsilon_2)^2+(\varepsilon_1-\varepsilon_3)^2+(\varepsilon_2-\varepsilon_3)^2]+\left(\frac{1}{\varepsilon_{yt}}-\frac{1}{\varepsilon_{yc}}\right)(\varepsilon_1+\varepsilon_2+\varepsilon_3)\geq 1 \tag{2.3}$$

Where, ε_{yt} and ε_{yc} are the tensile and compressive yield strains, and ε_1, ε_2, and ε_3 are the principal strains.

2.4.2.4 Maximum Principal Strain

The Maximum Principal Strain theory assumes failure occurs when one of the three principal strains equals or exceeds the strength [62]. Thus, failure occurs when,

$$\frac{\varepsilon_{yt}}{\varepsilon_1} \leq 1 \text{ or } \frac{\varepsilon_{yc}}{\varepsilon_3} \geq -1 \quad (2.4)$$

2.4.2.5 von Mises Strain

The von Mises strain failure criterion is a commonly used failure criterion for ductile engineering materials. It assumes yielding (i.e., failure) occurs when the distortion strain energy reaches or exceeds the distortion strain energy for yielding in tension or compression [62]. The von Mises strain criterion assumes failure occurs when:

$$\frac{\varepsilon_{yc}}{\varepsilon_{vm}} \leq 1 \quad (2.5)$$

Where, ε_{vm} is the von Mises strain and is calculated by the following equation.

$$\varepsilon_{vm} = \sqrt{\frac{1}{2}[(\varepsilon_1 - \varepsilon_2)^2 + (\varepsilon_1 - \varepsilon_3)^2 + (\varepsilon_2 - \varepsilon_3)^2]} \quad (2.6)$$

2.4.2.6 Tensile-Compressive Strength Ratio

The failure criteria we looked at depends on the strength of the bone material (e.g., tensile and compressive strength); however, in the literature there has been a variety of different tensile and compressive strengths reported for bone. For trabecular bone, Morgan et al. report an average compressive yield strain of approximately 7600 μstrain and an average tensile yield strain of approximately 6400 μstrain, resulting in a tensile-compressive strength ratio of 0.84 [66]. Higher compressive strain limits have been utilized in previous FE bone models, as a compressive strain limit of 11000 μstrain for trabecular bone has also been used in a previous distal radius FE study [60]. Ultimate tensile and compressive strain limits of 14100 and 23070, respectively, have also been reported for human trabecular bone, resulting in a strength ratio of 0.61 [67]. Previous studies have looked at the effect of different tensile-compressive strength ratios on the accuracy of their FE models [60,68]. Edwards and Troy recommend using a ratio of 0.5; however, Keyak et al. report that ratios less than 0.7 resulted in weaker failure theory performance when modeling bone as isotropic [60,68].

2.5 Summary

- Distal radius fracture is the most common type of osteoporotic fracture to occur in older adults, particularly postmenopausal women. This fracture typically occurs due to a fall on an outstretched hand, where the applied load exceeds the bone strength (i.e., failure load)
- HR-pQCT allows for 3D imaging of bone microarchitecture. When combined with FE analyses, HR-pQCT can non-invasively determine mechanical properties of the distal radius (e.g., failure load) *in vivo*. This is typically done by directly imaging and modeling a distal radius bone segment and applying axial compression until failure (as defined by the specified failure criterion). Failure loads obtained from HR-pQCT has been shown to be the strongest predictor of incident fracture risk at the radius in older adults
- Current HR-pQCT FE models simulate pure compressive (i.e., axial) loading conditions, neglecting off-axis loads (which create bending) that occur during a fall on an outstretched hand. Pure compressive HR-pQCT FE models explain 75% variance in experimental failure load, assuming failure occurs when 2% of all elements in the model exceed a critical strain threshold.
- Previous findings, based on a single participant, suggest that accounting for off-axis loading in distal radius FE models may be beneficial as off-axis failure loads were up to 47% lower than their respective axial failure loads. Thus, it could be possible to improve explained variance in HR-pQCT FE models by accounting for off-axis loads as well as considering other failure criterion and different percentages of failed tissue.

3 RESEARCH QUESTION AND OBJECTIVE

3.1 Research Question

This research hopes to address the following question: What moment arm combination best predicts off-axis experimental failure load with highest explained variance and least error in a HR-pQCT distal radius FE model?

3.2 Research Objective

To address this research question, the objective of this study was to identify moment arms in a HR-pQCT distal radius FE model that best predicted off-axis experimental failure load with highest explained variance and least error.

4 METHODOLOGY

4.1 HR-pQCT Imaging and Mechanical Testing

4.1.1 Specimens

We obtained 21 fresh-frozen human cadaveric forearms (mean donor age: 82.1; age range: 64-101 years) with all soft tissues intact. We selected specimens from donors without prior fractures or bone altering diseases and a BMI ranging between 18.5 and 25. We assumed that donors with a BMI < 18.5 were bedridden and would not be representative of a healthy population. Specimens were selected based on BMI (instead of wrist or radial BMD measures) since wrist BMD is not connected to osteoporosis diagnosis, as determined by DXA. Osteoporosis, defined by a T-score ≤ -2.5, is based on BMD measures obtained at the hip (i.e., femoral neck) or spine, not the wrist. Specimens were stored at -20°C [53-56] until approximately 20 hours prior to testing. Once thawed, imaging and testing were completed within 48-hours in order to minimize the number of freeze-thaw cycles. Although multiple freeze-thaw cycles do not affect mechanical properties of bone [53-56], it can alter mechanical properties of soft tissues [69,70].

4.1.2 Sample Preparation

Following the method outlined by Edwards and Troy [71], I removed all soft tissues in a section 6 to 12 cm proximal to the Lister's tubercle. I laid the palm of the hand flat against the counter surface and positioned pronated forearm at a 45° angle from the horizontal (Figure 4-1a). Although this step was not previously outlined in Edwards and Troy's method, I had positioned the forearm at this angle to ensure the specimen had correct radius and ulna orientations, as the radius rotates around the ulna during pronation. I used polymethylmethacrylate (PMMA) to secure the arm in this position. Once secured, continuing to follow the method outlined by Edwards and Troy [71], radial and ulnar osteotomies was performed 12 cm proximal to the Lister's tubercle. I then embedded the most proximal 6 cm in a gypsum potting material (Denstone), secured with PMMA inside a polyvinyl chloride (PVC) pipe (Figure 4-2). Dentstone was used to ensure that the specimen remained perpendicular in two planes during the experimental test; however, since Dentstone is a brittle material, PMMA was also used to ensure the embedded forearm bones remained fixed during the experiment.

Please note that Figures 4-1 and 4-2 show the methodology performed with an embalmed specimen - fresh-frozen specimens used in this study had soft tissue intact.

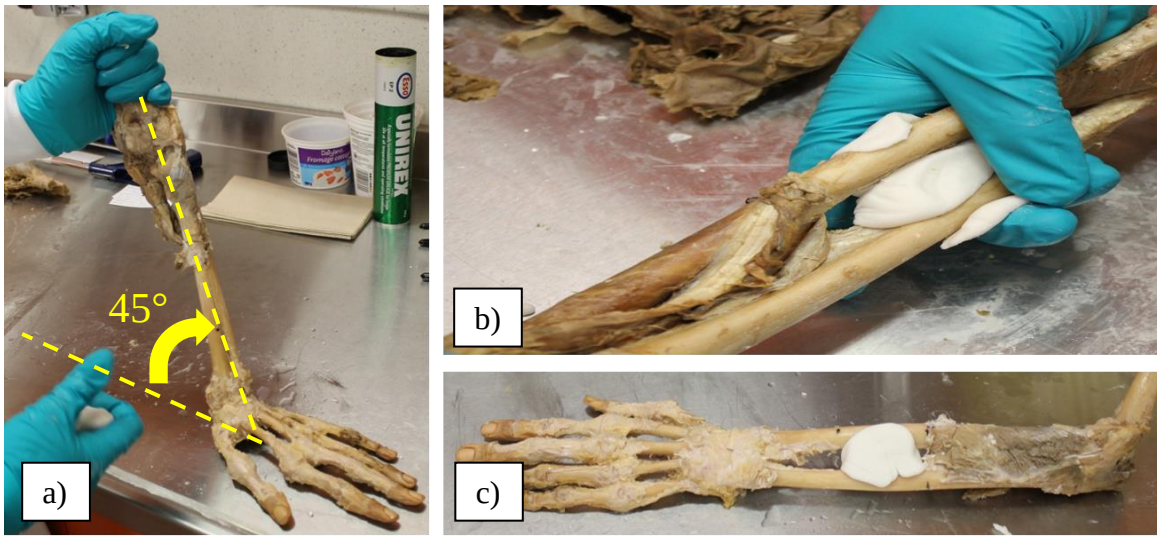

Figure 4-1. Methodology used to secure the arm into the falling position. a) The arm was positioned into the falling position by angling the forearm 45° above the horizontal; b) Secured the arm in the falling position using polymethylmethacrylate (PMMA); c) The secured arm. Note, images show an embalmed specimen being secured; however, I used fresh-frozen specimens that had soft tissue intact.

Figure 4-2. Potting specimens with Denstone and securing pot with a layer of polymethylmethacrylate (PMMA). Note, images show a potted embalmed specimen; however, I used fresh-frozen specimens that had soft tissue intact.

4.1.3 HR-pQCT Imaging and Analysis

Specimens were imaged using HR-pQCT (1st generation XtremeCT: Scanco Medical AG, Brüttisellen, Switzerland). We acquired standard clinical scans with a 9.02 mm (110 stacked CT images) region of interest (ROI), 9.5 mm proximal to the radial endplate with an isotropic voxel size of 82 µm. Scans were acquired at a voxel size of 82 µm as this is the standard method used in HR-pQCT imaging and many clinical studies acquired scans with this voxel size [59,72-76]. Measurement time for each scan was approximately 2.5 minutes.

One technician analyzed images using the manufacturer's standard evaluation (Scanco 64-bit Image Processing Language, v6.6). This evaluation was used to define the periosteal surface of the radius using a semi-automatic edge-finding algorithm and we modified the periosteal contour line when it deviated from the outer bone surface in the model. To identify bone voxels in the scan, the manufacturer's software automatically applied a fixed global threshold (400 mg HA/cm^3) during image processing [59]. From the HR-pQCT images and the Image Processing Language (IPL; version 1.15) software provided by Scanco, I obtained the centroid coordinates [mm].

4.1.4 Mechanical Testing

The testing configuration was set to simulate a fall on an outstretched hand. Specimens were tested in an off-axis loading configuration (15° dorsal inclination, 3-6° lateral inclination [30]) in a material testing system (MTS Bionix) (Figure 4-3; *Note, Figure 4-3 shows an embalmed specimen. Specimens used in this study had soft tissues intact*). Prior to failure testing, a 40 N preconditioning cyclic load was applied at a rate of 0.5 Hz for five minutes to reduce residual stresses and allow for repeatable, post-rigor muscle response [77]. Once preconditioned, the specimen was tested until failure by applying plate displacement at a rate of 3 mm/s [35]. During the test, load response and strain data were obtained at 1000 Hz using a data acquisition system (DAQ; National Instruments PXIe-1078 chassis with a PXIe-4300 voltage measurement).

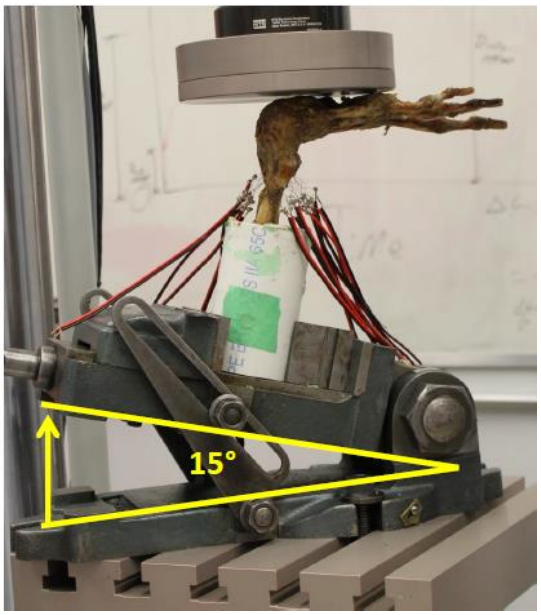

Figure 4-3. Testing configuration for off-axis loading, set to simulate a fall on an outstretched hand [27]. Note, the image shows an embalmed specimen; however, I used fresh-frozen specimens that had soft tissue intact.

4.2 Off-axis HR-pQCT FE Model

4.2.1 FE Model

Using manufacturer provided software (IPL), we created and solved subject-specific, homogenous FE models by converting each voxel in the HR-pQCT volume of interest into 8-node brick elements of the same size. I used a discrete, STM FE model and assigned an elastic modulus of 6.829 GPa and Poisson's ratio of 0.3 to all bone voxels in the model [23]. An elastic modulus of 6.829 GPa was used instead of 10 GPa as this is becoming the common approach when modeling HR-pQCT STM FE models [78,79]. I included a stiff, 8-voxel thick, plate with an elastic's modulus of 50 000 GPa and Poisson's ratio of 0.3 on the proximal face of the distal radius segment (Figure 4-4). The plate was included to apply off-axis loads and to prevent high localized stresses on individual trabeculae due to the applied nodal force. I determined plate properties by comparing failure loads obtained from an applied nodal force at the centroid and an offset to those obtained from standard compressive and bending loading conditions available in the IPL software [80].

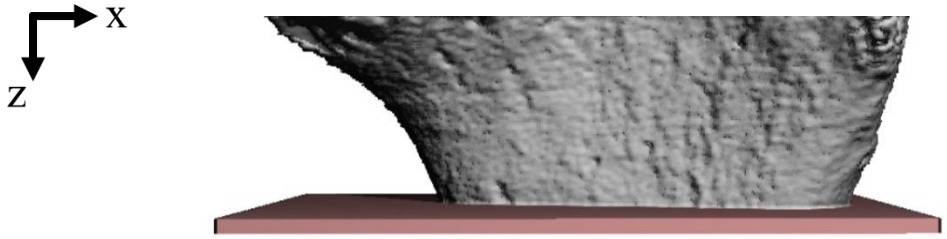

Figure 4-4. HR-pQCT off-axis model with the bone segment (grey) and stiff plate (pink)

4.2.2 Defining Magnitude of Moment Arms using Superposition

I determined moment arms in the x- and y-directions ($\bar{x}$, $\bar{y}$) for each HR-pQCT image in the ROI using a superposition method. Using the model developed in 4.2.1, I applied the following loading conditions (Figure 4-5):

1. Axial force applied at the centroid
2. Axial force applied at a 1 mm medial offset
3. Axial force applied at a 1 mm lateral offset
4. Axial force applied at a 1 mm dorsal offset

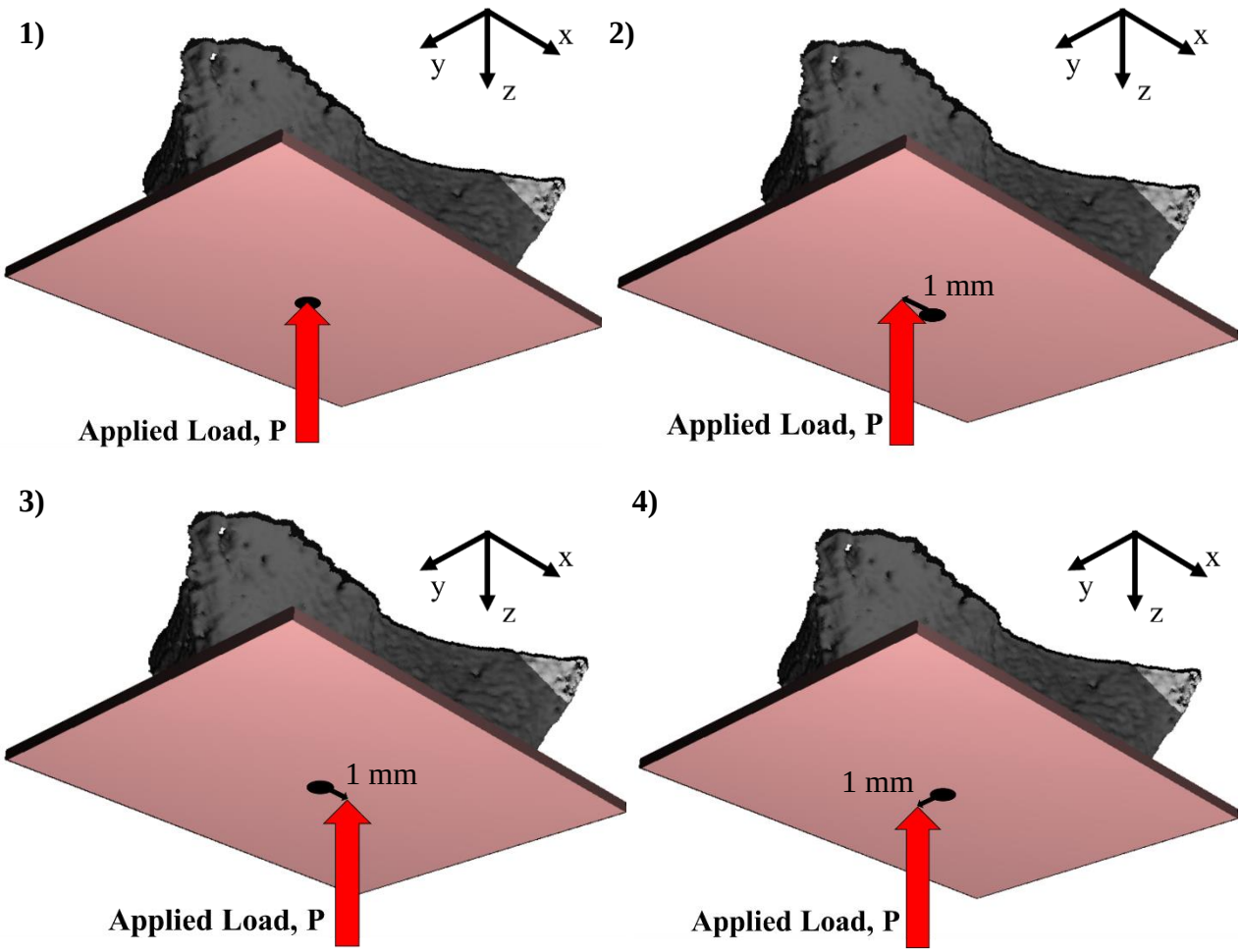

Figure 4-5. The four loading conditions applied in the HR-pQCT FE software to determine off-axis moment arms. An arbitrary axial nodal force is applied at the centroid *(1)* as well as at a 1 mm offset in the medial *(2)*, lateral *(3)*, and dorsal *(4)* direction.

Loading Conditions 2 to 4 have both a compressive component as well as a unit bending component due to the arbitrary load being applied at a 1 mm offset (Figure 4-6). Since the compressive component was known (as determined from Loading Condition 1), I determined the unit bending component in the medial, lateral, and dorsal directions by subtracting values obtained in Loading Condition 1 from Loading Conditions 2 to 4.

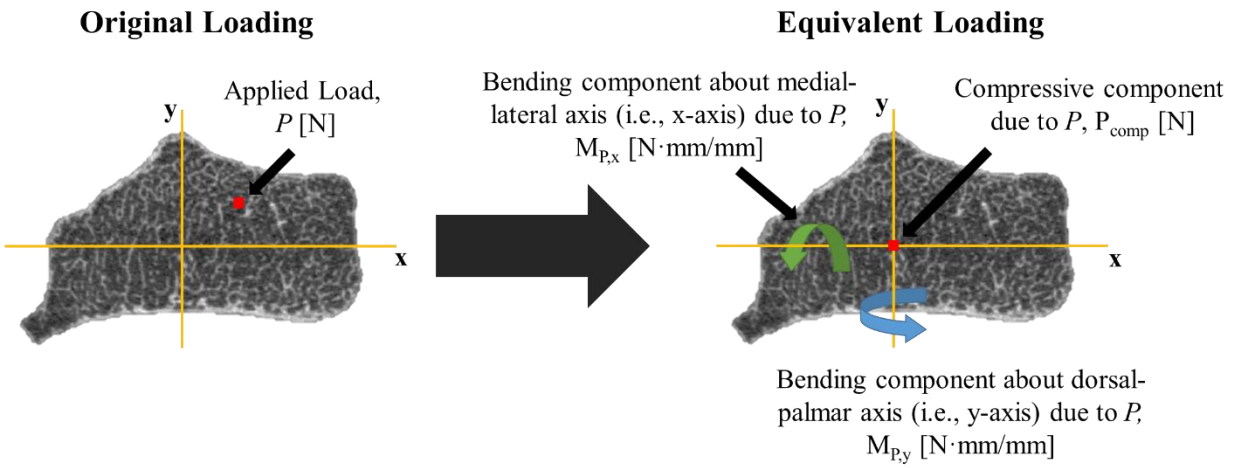

Figure 4-6. For an applied load located at a known offset from the centroid *(left)*, we can determine it's compressive and bending components due to the applied load *(right)*.

Once the unit bending components for a 1 mm offset in the medial, lateral, and dorsal directions were calculated, I used superposition (i.e., added compressive and bending components) to determine the predicted failure load at different medial-dorsal and lateral-dorsal moment arm combinations ($\bar{x}$, $\bar{y}$) by multiplying their respective unit bending component by the observed moment arm combination (Figure 4-7). I investigated different medial-dorsal and lateral-dorsal moment arm combinations in increments of 1 mm from 0 to 10 mm in either direction.

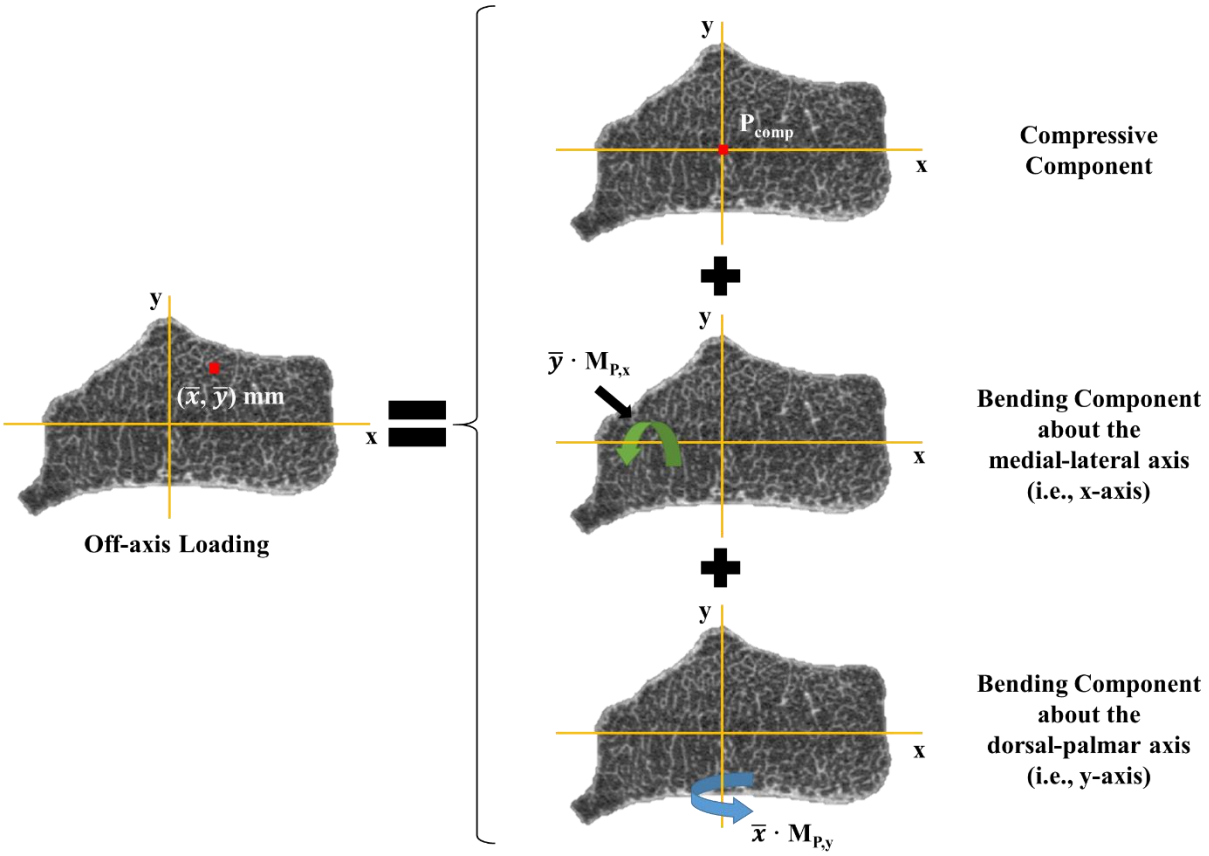

Figure 4-7. Superposition method of determining predicted off-axis failure load. At a given moment arm combination ($\bar{x}$, $\bar{y}$), we can model the statically-equivalent off-axis loading by adding the compressive component (P_{comp}), the bending component about the medial-lateral axis (i.e., x-axis) ($\bar{y} \cdot M_{P,x}$), and the bending component about the dorsal-palmar axis (i.e., y-axis) ($\bar{x} \cdot M_{P,y}$), where $M_{P,x}$ is the unit bending component for 1 mm offset in dorsal direction and $M_{P,y}$ is the unit bending component for a 1 mm offset in the medial or lateral direction.

The predicted failure load at each moment arm combination were obtained by scaling the applied force by their respective safety factor (Equation 4.1). This safety factor corresponded to the point where a defined percentage of all elements failed or a defined fixed volume of elements failed, according to a given failure criterion. For example, if 2% of all elements failing resulted in a safety factor of 0.5 with an applied load of 9000 N, from Equation 7, the predicted failure load would be 4500 N. I considered failed percentages of 0.1% to 10%, in increments of 0.5%, and failed fixed volumes of 1 mm^3 to 450 mm^3, in increments of 50 mm^3 [25,60]. I looked at various failure criteria (Table 2-1; pg. 16), as previously mentioned. I assumed a tensile yield strain limit of 7000 μstrain, which is commonly used in HR-pQCT FE models, and assumed a tensile-compressive strength ratio of 0.7 [52,68].

$$Predicted\ Failure\ Load = Applied\ Load\ \cdot\ Safety\ Factor \quad (4.1)$$

4.3 Statistical Analysis

Linear regressions were used to determine a failure criterion that maximized coefficients of determination (R^2) between predicted off-axis failure loads and experimental failure loads, where the predicted off-axis failure load was defined as the independent variable and the experimental failure load was defined as the dependent variable. For each failure criterion, I determined the R^2 (i.e., explained variance) at each moment arm combination. I then compared the different R^2 values obtained to determine which failure criterion and moment arm combination had the highest explained variance.

Prediction error was assessed using root mean squared error normalized in relation to maximum measured failure load (RMSE%), between predicted off-axis failure loads and experimental failure load. I selected the moment arm combination and failure criterion that had the least amount of prediction error. Statistical analysis was performed using MATLAB R2018b (Mathworks Inc.).

5 RESULTS

5.1 Experimental Data

Sixteen specimens had a distal radius fracture, four had a radius fracture that originated at the potting, and one had a scaphoid fracture. Since we were primarily investigating distal radius fractures in our study, we only considered specimens that had a distal radius fracture in our analysis. Our mean experimental off-axis failure load was 744 (SD 311) N. Load-displacement curves generated for each specimen can be seen in Appendix A.

5.2 Comparison between Experimental and Predicted Failure Loads

The moment arm (i.e., loading scenario) that best predicted experimental failure load with highest explained variance and lowest RMSE% was at a 1 mm dorsal offset. We show highest explained variance and lowest RMSE% for its respective percentage-based critical volume (V_{crit}) for ε_{eff}, ε_{hoff}, ε_{max} and ε_{vm} in Table 5-1. We obtained similar results with fixed volume-based critical volumes (*not reported*). In general, highest explained variance and low RMSE% were obtained using the von Mises strain failure criterion (Table 5-1; Figure 5-1). With this failure criterion, a 1 mm dorsal offset loading scenario explained approximately 80% variance in experimental failure load with RMSE% values ranging between 24% to 79%.

In terms of previous recommendations, pure compressive loading explained 70% to 77% variance in experimental failure load with RMSE% values ranging between 27% to 80%; the previously recommended loading scenario for off-axis loading (8 mm medial offset, 7 mm dorsal offset [26]) explained 24% to 30% variance in experimental failure load with RMSE% values between 25% and 30%.

Plots of explained variance and RMSE% values obtained for the other failure criterion considered in this study can be seen in Appendix B.

Table 5-1. Prediction error (i.e., RMSE%) and explained variance (i.e., R^2) between predicted and experimental failure load for axial and off-axis loading. For off-axis loading, results were presented for the current recommended moment arms [26] as well as for a 1 mm dorsal moment arm, which provided the highest explained variance and least error in this study.

Failure Criteria	**Axial Loading**			**Off-axis Loading**					
				1 mm Dorsal			8 mm Medial, 7 mm Dorsal [26]		
	V_{crit}	R^2	*RMSE%*	V_{crit}	R^2	*RMSE%*	V_{crit}	R^2	*RMSE%*
ε_{eff}	3.5%	0.75	89%	1.0%	0.79	65%	0.5%	0.29	25%
ε_{hoff}	4.5%	0.76	87%	0.5%	0.80	52%	2.0%	0.28	24%
ε_{max}	2.0%	0.74	136%	0.1%	0.79	78%	0.1%	0.27	26%
ε_{vm}	2.5%	0.75	54%	1.0%	0.79	42%	2.0%	0.28	25%

a) 1 mm Dorsal Offset

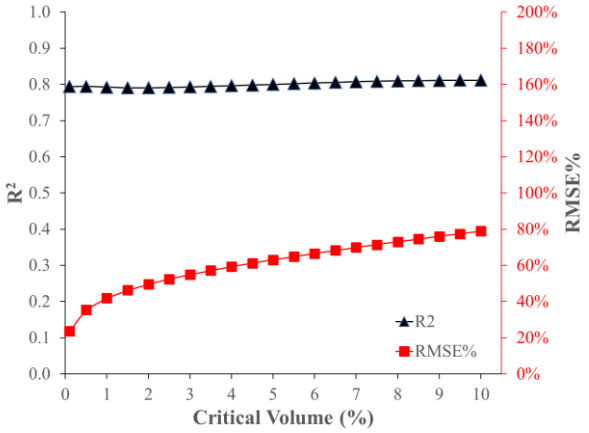

b) Pure Compression

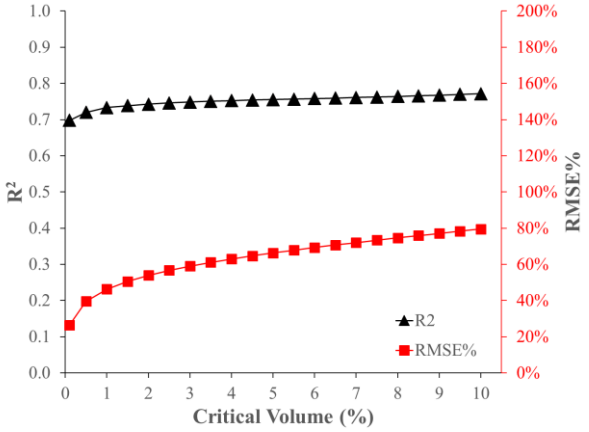

c) (8,7) mm Medial-Dorsal Offset

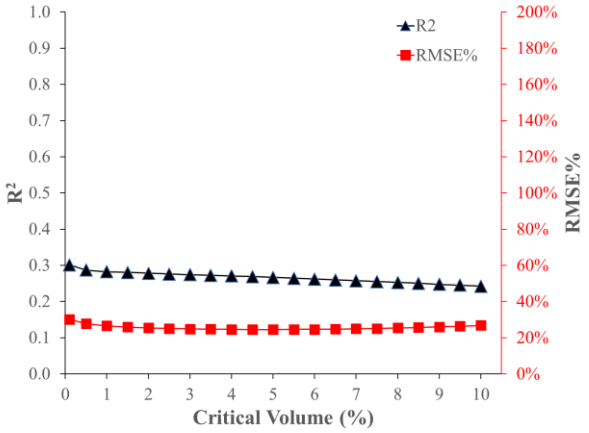

Figure 5-1. Changes in explained variance (R^2; black) and root mean squared error percentage (RMSE%; red) for a percentage-based critical volume. Results were obtained for the von Mises failure criterion.

6 DISCUSSION

The objective of this study was to identify moment arms in a HR-pQCT distal radius FE model that best predicted off-axis experimental failure load with highest explained variance and least error. Our findings indicate that it may be beneficial to apply a 1 mm dorsal offset in HR-pQCT off-axis FE models, as this loading scenario explained 79% variance in experimental failure load, a 4% improvement relative to the axial loading scenario; however, RMSE% appeared high for both scenarios (1 mm offset: 42%; axial loading: 51%).

In general, the von Mises strain failure criterion best predicted experimental failure load as it had the lowest RMSE% values, relative to the other failure criterion we investigated in this study. This finding differs from previous studies where they found that the Hoffman stress and von Mises stress criterion best predicted fracture strength of the distal radius and proximal femur, respectively [60,68]. This discrepancy in failure criterion performance could be due to the differing FE models, as these previous studies modeled intact bones whereas we modeled a segment of the distal radius imaged using HR-pQCT. By only modeling the bone segment, we were limited in the simulated load transition through the radius (in contrast to Edward and Troy's intact distal radius FE model [60]), possibly affecting the performance of the different failure criterion investigated. It should be noted that Keyak and Rossi did not account for prediction error in their study [68], which could be another potential reason why failure criterion performance differed between studies.

In general, we observed large RMSE% values for the various loading scenarios as our model consistently overestimated predicted distal radius failure load, indicating that our off-axis HR-pQCT model was not accurate. This issue, however, is also apparent in the current HR-pQCT FE model that simulates pure compressive loading, as predicted failure load from the current model overestimated experimental failure loads by 29% [52]. A possible reason for the observed large RMSE% values could be due to partial volume effects, as all our models utilized an 82 µm voxel size. It may be possible to improve our RMSE% values by implementing a different FE modeling approach, such as the method described by Hosseini et al. [50]. In this method, the HR-pQCT volume of interest was coarsened from a voxel size of 82 µm to 1.0 mm. The resulting coarsened image was converted into a FE model, meshed using hexahedral elements with an edge length of 1.0 mm, and assigned anisotropic material properties [50]. It is possible that utilizing anisotropic, 1.0 mm elements in contrast to the isotropic, 82 µm elements we utilized in this study will improve our model's accuracy. It may also be possible to improve our RMSE% by adjusting the tolerances

implemented in the FE convergence criterion, since applying a smaller tolerance to the force and displacement convergence criterion it may improve model accuracy.

We observed lower explained variance at moment arms further away from the centroid, indicating that a fall configuration tested was primarily compressive in nature. Troy and Grabiner suggest that stabilization of the wrist may reduce the effects of off-axis loading on the radius, resulting in a more compressive loading scenario [8]. Their simulation, however, did not account for this effect on loading of the radius as they did not model soft tissue in their model and could have overestimated the degree at which off-axis loads could reduce the failure load of the radius. This could potentially also be the reason why we only observed a 4% difference in explained variance between off-axis and axial loading. Although we also did not include soft tissue in our models, we did use fresh-frozen cadaveric forearms when obtaining experimental failure loads and would have inherently accounted for the effects of intact wrist ligaments on off-axis load reduction in our experimental setup.

In the current study, we focused solely on distal radius fractures as we excluded specimens that did not experience a distal radius fracture (e.g., scaphoid fracture); however, there is some opportunity to investigate other fracture types. Although scaphoid fractures are the most common carpal fracture to occur during a fall on an outstretched hand, accounting for 79% of all carpal fractures [81], they are difficult to assess in an experimental setting due to physical limitations in the methodology. In order to further investigate scaphoid fractures, we would need to experimentally assess the load response of the scaphoid via strain gauges; however, attaching strain gauges to the scaphoid would be physically challenging. There is, however, still an opportunity to develop testing methodologies and investigate other fractures types as most testing methodologies focus primarily on distal radius fractures [19,30]. For example, prospective work could assess distal ulna fractures as well since they mostly occur with a distal radius fracture [82] and load sharing does occur between the radius and ulna when the forearm is loaded [83-88].

This research has strengths that warrant discussion. First, we used intact forearms when simulating a fall on an outstretched hand in our mechanical tests, resulting in clinically comparable distal radius fractures [19]. Unlike excised radius studies, this allowed us to simulate loading conditions that are more representative of *in vivo* conditions since we include other tissues and bones that contribute to loading. Second, our use of fresh-frozen cadaveric specimens avoided negative mechanical property variation induced by embalming [89]. Third, we obtained specimens

exclusively from older female donors, allowing us to focus on a population that are prone to fractures [4].

There are also some limitations with this research that need to be discussed. First, our results may be limited by our 16 specimens with similar sizes and should be confirmed with a larger and more varied sample size. It may be possible to obtain a larger failure load range with specimens of varied sizes, as we observed a small range in obtained failure load in this study. Second, we utilized a slow displacement rate (3 mm/s) in our mechanical tests, which differs from rates experienced during a fall (>1 m/s) [90]; however, other groups have shown that this displacement rate can successfully create clinically comparable distal radius fractures [7,25,60]. In relation to our FE model, by not incorporating the dynamic loading the radius experiences during a fall, we neglected the inertial force associated with dynamic loading in the current study. Third, our models had much longer convergence times than the standard HR-pQCT discrete FE models (~10-15 hrs vs. ~3 hrs), limiting their feasibility for clinical use. This longer convergence time could potentially be due to the millions of additional elements added for the stiff plate in our model. It may be possible to reduce this time by increasing the element size of the stiff plate, which is currently 82 µm. Fourth, our FE models assumed fixed, homogenous material properties for cortical and trabecular bone. It may be beneficial for future studies to consider utilizing density-modulus relations in our models to account for differences in tissue mineralization; however, this will also further increase the convergence times of these models. Fifth, we only modeled a segment of the radius instead of the whole bone in our FE analysis. While it may be beneficial to model the whole bone, focusing on the radial segment captured by a clinical HR-pQCT scan allows for thousands of clinical HR-pQCT scans that have been previously obtained in the literature to be reanalyzed using the off-axis FE method outlined in this study. Sixth, there is bias in our findings as our models overestimated predicted distal radius failure load. It may be possible to account for this bias by considering other failure criteria and adjusting the failure criterion utilized. Seventh, we did not account for the ulna when assessing failure load, although some load sharing does occur between the radius and ulna when loaded [83-88].

7 CONCLUSION

7.1 Overview

The current HR-pQCT based FE model has been used in several studies to predict intact forearm failure load as a replacement for other image-based indices, such as BMD. Although this FE model has improved distal radius failure load predictions, it is still limited as it does not account for off-axis loading that would occur during a fall on an outstretched hand. This research aims to address this limitation by accounting for off-axis loading through the identification of moment arms in a HR-pQCT distal radius FE model that best predicted off-axis experimental failure load with highest explained variance and least error.

We found that it may be beneficial to apply a 1 mm dorsal offset in HR-pQCT off-axis FE models, as this loading scenario explained 79% variance in experimental failure load for a 1.0% critical volume, specifically when using von Mises strain criterion. However, our model at this loading scenario was not accurate, as we observed an RMSE% of 42% due to the overestimation of predicted radius failure load. This overestimation is an inherent issue in current HR-pQCT FE models as the commonly used HR-pQCT FE model that simulates pure compressive loading also overestimated predicted failure loads [52]. At the 1 mm dorsal offset, explained variance was 4% higher than the axial loading scenario and 51% higher than the current recommended off-axis loading scenario.

7.2 Contributions

There are some contributions from this study that can be discussed. First, the results from this study suggest that incorporating off-axis loading in HR-pQCT FE models modestly improved (4%) explained variance in experimental failure load. Second, we provide an off-axis loading scenario that is specific to HR-pQCT images and based on a larger sample size than previous off-axis studies [8,26]. Previous models that incorporate off-axis loading were based off of other imaging modalities and based on a scan from a single participant [8].

7.3 Clinical Significance

By identifying the best moment arm combination to apply when assessing off-axis loading in HR-pQCT FE models, we could potentially allow for more accurate predictions of distal radius failure load to be available for patients and clinicians. This is because an off-axis model will consider bending moments that are not accounted for in current HR-pQCT FE models, which simulate pure compression [52]. Improved predictions of distal radius failure load *in vivo*, can be particularly

beneficial in populations where individuals are at higher risk for fracture (e.g., postmenopausal women). Improved distal failure load predictions, in conjunction with predicted impact load experienced by the radius during a fall (based on height, weight, and sex), can be used to determine a more accurate estimation of an individual's fracture risk (i.e., safety factor). A more accurate HR-pQCT FE model can also evaluate future interventions (e.g., medication, diet, exercise) by assessing predicted distal radius failure load and fracture prevention.

Although our approach to modeling off-axis in HR-pQCT FE models assumes the same 1 mm dorsal offset is applicable to all patients or subjects, this may not be the case. It may be beneficial for prospective studies to investigate an approach of reporting moment arms that are subject-specific (i.e., the moment arm combination will correspond to the simulated off-axis loading scenario at which the radius is at its weakest), as this method may be more clinically relevant.

7.4 Future Work

- Future work can include specimens from donors of different ages, sizes, and frailty status, as donors for this work were exclusively older women. This would allow this work to be applied to a broader population.
- It may be beneficial to consider 0.5 mm increments when investigating different moment arm combination in future work, as we had only considered 1 mm increments in the current study.
- To improve predictions of distal radius failure, it may be beneficial to incorporate a cluster analysis in future work. This means that a volume of contiguous elements must fail in order to assume the entire model has failed (e.g., a cluster of elements where the volume corresponds to 2% of all elements). In contrast, the current study assumes that as long as the number of elements failed meets the failure criteria (e.g., 2% of all elements), irrespective of the element's location, the model is considered to have failed. This approach has been used by others to predict fracture strength of the distal radius [8,60] and proximal femur [68,91].
- Develop a method of identifying subject-specific moment arm combinations when predicting HR-pQCT based off-axis distal radius failure load. This approach may be more clinically relevant since the HR-pQCT FE model would simulate an off-axis loading scenario that is specific to the individual.

REFERENCES

1. Bouillon R, Burckhardt P, Christiansen C, Fleisch HA, Fujita T, Gennari C, et al. Consensus development conference: prophylaxis and treatment of osteoporosis. Osteoporos Int. Feb 1991;1(2):114-7.
2. Cummings SR, Melton LJ. Epidemiology and outcomes of osteoporotic fractures. Lancet (London, England). May 18 2002;359(9319):1761-7.
3. Johnell O, Kanis JA. An estimate of the worldwide prevalence and disability associated with osteoporotic fractures. Osteoporos Int. Dec 2006;17(12):1726-33.
4. Cuddihy MT, Gabriel SE, Crowson CS, O'Fallon WM, Melton LJ, 3rd. Forearm fractures as predictors of subsequent osteoporotic fractures. Osteoporosis International. 1999;9:469-75.
5. Mallmin H, Ljunghall S, Persson I, Naessen T, Krusemo U-B, Bergstrom R. Fracture of the distal forearm as a forecaster of subsequent hip fracture: a population-based cohort study with 24 years follow-up. Calcified tissue international. 1993;52:269-72.
6. van Rietbergen B, Ito K. A survey of micro-finite element analysis for clinical assessment of bone strength: The first decade. Journal of Biomechanics. 2015/03/18/ 2015;48(5):832-41.
7. Pistoia W, van Rietbergen B, Lochmuller EM, Lill CA, Eckstein F, Ruegsegger P. Estimation of distal radius failure load with micro-finite element analysis models based on three-dimensional peripheral quantitative computed tomography images. Bone. 2002;30(6):842-8.
8. Troy KL, Grabiner MD. Off-axis loads cause failure of the distal radius at lower magnitudes than axial loads: a finite element analysis. Journal of biomechanics. 2007;40(8):1670-5.
9. Martini F. Human anatomy. 7th ed.. ed. Timmons MJ, Tallitsch RB, editors. Boston: Boston : Benjamin Cummings; 2012.
10. Marieb EN. Human anatomy & physiology. New York: Pearson Education; 2004.
11. Spadaro JA, Werner FW, Brenner RA, Fortino MD, Fay LA, Edwards WT. Cortical and trabecular bone contribute strength to the osteopenic distal radius. Journal of Orthopaedic Research. 1994;12(2):211-8.

12. Augat P, Claes LE. Prediction of fracture load at different skeletal sites by geometric properties of the cortical shell. Journal of Bone and Mineral Research. 1996;11(9):1356-63.
13. Augat P, Schorlemmer S. The role of cortical bone and its microstructure in bone strength. Age Ageing. Sep 2006;35 Suppl 2:ii27-ii31.
14. Oftadeh R, Perez-Viloria M, Villa-Camacho JC, Vaziri A, Nazarian A. Biomechanics and Mechanobiology of Trabecular Bone: A Review. Journal of biomechanical engineering. 1372015. p. 0108021-01080215.
15. van Lenthe GH, Muller R. CT-based visualization and quantification of bone microstructure in vivo. IBMS BoneKEy. 10.1138/20080348 11/00/online 2008;5(11):410-25.
16. Leslie WD, Morin SN. Osteoporosis epidemiology 2013: implications for diagnosis, risk assessment, and treatment. Current opinion in rheumatology. 2014;26(4):440-6.
17. Burge R, Dawson-Hughes B, Solomon DH, Wong JB, King A, Tosteson A. Incidence and Economic Burden of Osteoporosis-Related Fractures in the United States, 2005–2025. Journal of Bone and Mineral Research. 2007;22(3):465-75.
18. Kanis JA, Johnell O, De Laet C, Johansson H, Oden A, Delmas P, et al. A meta-analysis of previous fracture and subsequent fracture risk. Bone. Aug 2004;35(2):375-82.
19. Wagner DW, Lindsey DP, Beaupre GS. Replicating a Colles fracture in an excised radius: revisiting testing protocols. Journal of biomechanics. Apr 5 2012;45(6):997-1002.
20. Adam MJ, Amini M, Johnston G, Kontulainen SA, Johnston JD. Distal radius strain distributions during off-axis loading. Alberta Biomedical Engineering Conference; Banff, AB 2014.
21. Melton LJ, 3rd, Christen D, Riggs BL, Achenbach SJ, Muller R, van Lenthe GH, et al. Assessing forearm fracture risk in postmenopausal women. Osteoporosis International. Jul 2010;21(7):1161-9.
22. Pistoia W, van Rietbergen B, Lochmuller EM, Lill CA, Eckstein F, Ruegsegger P. Image-based micro-finite-element modeling for improved distal radius strength diagnosis: moving from bench to bedside. J Clin Densitom. Summer 2004;7(2):153-60.

23. Macneil JA, Boyd SK. Bone strength at the distal radius can be estimated from high-resolution peripheral quantitative computed tomography and the finite element method. Bone. Jun 2008;42(6):1203-13.
24. Varga P, Pahr DH, Baumbach S, Zysset PK. HR-pQCT based FE analysis of the most distal radius section provides an improved prediction of Colles' fracture load in vitro. Bone. Nov 2010;47(5):982-8.
25. Mueller TL, Christen D, Sandercott S, Boyd SK, van Rietbergen B, Eckstein F, et al. Computational finite element bone mechanics accurately predicts mechanical competence in the human radius of an elderly population. Bone. Jun 1 2011;48(6):1232-8.
26. Troy KL, Scerpella TA, Dowthwaite JN. Circum-menarcheal bone acquisition is stress-driven: A longitudinal study in adolescent female gymnasts and non-gymnasts. J Biomech. Sep 10 2018;78:45-51.
27. McDonald MP. Predicting Distal Radius Failure Load during a Fall using Mechanical Testing and Peripheral Quantitative Computed Tomography. University of Saskatchewan; 2017.
28. Kanis JAobotWHOSG. Assessment of osteoporosis at the primary health-care level. World Health Organization Collaborating Centre for Metabolic Bone Diseases. Technical Report 2007.
29. Hudelmaier M, Kuhn V, Lochmuller EM, Well H, Priemel M, Link TM, et al. Can geometry-based parameters from pQCT and material parameters from quantitative ultrasound (QUS) improve the prediction of radial bone strength over that by bone mass (DXA)? Osteoporos Int. May 2004;15(5):375-81.
30. Muller ME, Webber CE, Bouxsein ML. Predicting the failure load of the distal radius. Osteoporos Int. Jun 2003;14(4):345-52.
31. Ammann P, Rizzoli R. Bone strength and its determinants. Osteoporos Int. 2003;14 Suppl 3:S13-8.
32. Ward KA, Link TM, Adams JE. Tools for Measuring Bone in Children and Adolescents. In: Fung EB, Bachrach LK, Sawyer AJ, editors. Bone Health Assessment in Pediatrics: Guidelines for Clinical Practice. Cham: Springer International Publishing; 2016. p. 23-52.

33. Kawalilak CE, Bunyamin AT, Bjorkman KM, Johnston JD, Kontulainen SA. Precision of bone density and micro-architectural properties at the distal radius and tibia in children: an HR-pQCT study. Osteoporos Int. Nov 2017;28(11):3189-97.
34. Augat P, Iida H, Jiang Y, Diao E, Genant HK. Distal radius fractures: mechanisms of injury and strength prediction by bone mineral assessment. Journal of orthopaedic research : official publication of the Orthopaedic Research Society. Sep 1998;16(5):629-35.
35. Lochmuller EM, Lill CA, Kuhn V, Schneider E, Eckstein F. Radius bone strength in bending, compression, and falling and its correlation with clinical densitometry at multiple sites. Journal of bone and mineral research : the official journal of the American Society for Bone and Mineral Research. Sep 2002;17(9):1629-38.
36. Hosseinitabatabaei S. High-Resolution peripheral Quantitative Computed Tomography Based Finite Element Modelling of Distal Radius Strength: Assessing Effect of Heterogeneous Material Properties and Scan Site. Biomedical Engineering. Saskatoon, SK, CAN: University of Saskatchewan; 2018.
37. Agarwal S, Rosete F, Zhang C, McMahon DJ, Guo XE, Shane E, et al. In vivo assessment of bone structure and estimated bone strength by first- and second-generation HR-pQCT. Osteoporosis International. journal article October 01 2016;27(10):2955-66.
38. Farr JN, Amin S, Melton LJ, 3rd, Kirmani S, McCready LK, Atkinson EJ, et al. Bone strength and structural deficits in children and adolescents with a distal forearm fracture resulting from mild trauma. Journal of bone and mineral research : the official journal of the American Society for Bone and Mineral Research. Mar 2014;29(3):590-9.
39. Maatta M, Macdonald HM, Mulpuri K, McKay HA. Deficits in distal radius bone strength, density and microstructure are associated with forearm fractures in girls: an HR-pQCT study. Osteoporos Int. Mar 2015;26(3):1163-74.
40. Macdonald HM, Maatta M, Gabel L, Mulpuri K, McKay HA. Bone Strength in Girls and Boys After a Distal Radius Fracture: A 2-Year HR-pQCT Double Cohort Study. J Bone Miner Res. Feb 2018;33(2):229-40.
41. Kirmani S, Christen D, van Lenthe GH, Fischer PR, Bouxsein ML, McCready LK, et al. Bone structure at the distal radius during adolescent growth. Journal of bone and mineral research : the official journal of the American Society for Bone and Mineral Research. Jun 2009;24(6):1033-42.

42. Dimitri P, Jacques RM, Paggiosi M, King D, Walsh J, Taylor ZA, et al. Leptin may play a role in bone microstructural alterations in obese children. The Journal of clinical endocrinology and metabolism. Feb 2015;100(2):594-602.
43. Farr JN, Amin S, LeBrasseur NK, Atkinson EJ, Achenbach SJ, McCready LK, et al. Body composition during childhood and adolescence: relations to bone strength and microstructure. The Journal of clinical endocrinology and metabolism. Dec 2014;99(12):4641-8.
44. Faje AT, Karim L, Taylor A, Lee H, Miller KK, Mendes N, et al. Adolescent girls with anorexia nervosa have impaired cortical and trabecular microarchitecture and lower estimated bone strength at the distal radius. The Journal of clinical endocrinology and metabolism. May 2013;98(5):1923-9.
45. Chevalley T, Bonjour JP, van Rietbergen B, Ferrari S, Rizzoli R. Fractures during childhood and adolescence in healthy boys: relation with bone mass, microstructure, and strength. The Journal of clinical endocrinology and metabolism. Oct 2011;96(10):3134-42.
46. Chevalley T, Bonjour JP, van Rietbergen B, Ferrari S, Rizzoli R. Tracking of environmental determinants of bone structure and strength development in healthy boys: an eight-year follow up study on the positive interaction between physical activity and protein intake from prepuberty to mid-late adolescence. Journal of bone and mineral research : the official journal of the American Society for Bone and Mineral Research. Oct 2014;29(10):2182-92.
47. Chevalley T, Bonjour JP, van Rietbergen B, Rizzoli R, Ferrari S. Fractures in healthy females followed from childhood to early adulthood are associated with later menarcheal age and with impaired bone microstructure at peak bone mass. The Journal of clinical endocrinology and metabolism. Nov 2012;97(11):4174-81.
48. Nishiyama KK, Macdonald HM, Moore SA, Fung T, Boyd SK, McKay HA. Cortical porosity is higher in boys compared with girls at the distal radius and distal tibia during pubertal growth: an HR-pQCT study. Journal of bone and mineral research : the official journal of the American Society for Bone and Mineral Research. Feb 2012;27(2):273-82.
49. Samelson EJ, Broe KE, Xu H, Yang L, Boyd S, Biver E, et al. Cortical and trabecular bone microarchitecture as an independent predictor of incident fracture risk in older women and

men in the Bone Microarchitecture International Consortium (BoMIC): a prospective study. The Lancet Diabetes & Endocrinology. 2019;7(1):34-43.

50. Hosseini HS, Dunki A, Fabech J, Stauber M, Vilayphiou N, Pahr D, et al. Fast estimation of Colles' fracture load of the distal section of the radius by homogenized finite element analysis based on HR-pQCT. Bone. Apr 2017;97:65-75.
51. Varga P, Dall'Ara E, Pahr DH, Pretterklieber M, Zysset PK. Validation of an HR-pQCT-based homogenized finite element approach using mechanical testing of ultra-distal radius sections. Biomechanics and modeling in mechanobiology. Jul 2011;10(4):431-44.
52. Pistoia W, van Rietbergen B, Lochmuller EM, Lill CA, Eckstein F, Ruegsegger P. Estimation of distal radius failure load with micro-finite element analysis models based on three-dimensional peripheral quantitative computed tomography images. Bone. Jun 2002;30(6):842-8.
53. Borchers RE, Gibson LJ, Burchardt H, Hayes WC. Effects of selected thermal variables on the mechanical properties of trabecular bone. Biomaterials. May 1995;16(7):545-51.
54. Goh JC, Ang EJ, Bose K. Effect of preservation medium on the mechanical properties of cat bones. Acta orthopaedica Scandinavica. Aug 1989;60(4):465-7.
55. Linde F, Sorensen HC. The effect of different storage methods on the mechanical properties of trabecular bone. Journal of biomechanics. Oct 1993;26(10):1249-52.
56. Sedlin ED. A rheologic model for cortical bone. A study of the physical properties of human femoral samples. Acta orthopaedica Scandinavica Supplementum. 1965:Suppl 83:1-77.
57. Engelke K, van Rietbergen B, Zysset P. FEA to measure bone strength: a review. Clinical reviews in bone and mineral metabolism. 2016;14(1):26-37.
58. Vilayphiou N, Boutroy S, Sornay-Rendu E, Van Rietbergen B, Munoz F, Delmas PD, et al. Finite element analysis performed on radius and tibia HR-pQCT images and fragility fractures at all sites in postmenopausal women. Bone. Apr 2010;46(4):1030-7.
59. Kawalilak CE, Kontulainen SA, Amini MA, Lanovaz JL, Olszynski WP, Johnston JD. In vivo precision of three HR-pQCT-derived finite element models of the distal radius and tibia in postmenopausal women. BMC musculoskeletal disorders. Sep 13 2016;17(1):389.
60. Edwards WB, Troy KL. Finite element prediction of surface strain and fracture strength at the distal radius. Medical engineering & physics. Apr 2012;34(3):290-8.

61. Hoffman O. The Brittle Strength of Orthotropic Materials. Journal of Composite Materials. 1967/04/01 1967;1(2):200-6.
62. Budynas R, Nisbett JK, Shigley JE. Shigley's mechanical engineering design. 2015.
63. Niebur GL, Feldstein MJ, Yuen JC, Chen TJ, Keaveny TM. High-resolution finite element models with tissue strength asymmetry accurately predict failure of trabecular bone. Journal of biomechanics. Dec 2000;33(12):1575-83.
64. Verhulp E, Van Rietbergen B, Muller R, Huiskes R. Micro-finite element simulation of trabecular-bone post-yield behaviour--effects of material model, element size and type. Comput Methods Biomech Biomed Engin. Aug 2008;11(4):389-95.
65. Ohman C, Dall'Ara E, Baleani M, Van Sint Jan S, Viceconti M. The effects of embalming using a 4% formalin solution on the compressive mechanical properties of human cortical bone. Clin Biomech (Bristol, Avon). Dec 2008;23(10):1294-8.
66. Morgan EF, Keaveny TM. Dependence of yield strain of human trabecular bone on anatomic site. J Biomech. May 2001;34(5):569-77.
67. Rincón-Kohli L, Zysset PK. Multi-axial mechanical properties of human trabecular bone. Biomechanics and Modeling in Mechanobiology. 2009/06/01 2009;8(3):195-208.
68. Keyak JH, Rossi SA. Prediction of femoral fracture load using finite element models: an examination of stress- and strain-based failure theories. J Biomech. Feb 2000;33(2):209-14.
69. Changoor A, Fereydoonzad L, Yaroshinsky A, Buschmann MD. Effects of refrigeration and freezing on the electromechanical and biomechanical properties of articular cartilage. Journal of biomechanical engineering. Jun 2010;132(6):064502.
70. Huang H, Zhang J, Sun K, Zhang X, Tian S. Effects of repetitive multiple freeze-thaw cycles on the biomechanical properties of human flexor digitorum superficialis and flexor pollicis longus tendons. Clinical biomechanics (Bristol, Avon). May 2011;26(4):419-23.
71. Edwards WB, Troy KL. Simulating distal radius fracture strength using biomechanical tests: a modeling study examining the influence of boundary conditions. Journal of biomechanical engineering. Nov 2011;133(11):114501.
72. Cheung AM, Adachi JD, Hanley DA, Kendler DL, Davison KS, Josse R, et al. High-resolution peripheral quantitative computed tomography for the assessment of bone

strength and structure: a review by the Canadian Bone Strength Working Group. Current Osteoporosis Reports. Jun 2013;11(2):136-46.

73. Boutroy S, Van Rietbergen B, Sornay-Rendu E, Munoz F, Bouxsein ML, Delmas PD. Finite element analysis based on in vivo HR-pQCT images of the distal radius is associated with wrist fracture in postmenopausal women. Journal of bone and mineral research : the official journal of the American Society for Bone and Mineral Research. Mar 2008;23(3):392-9.
74. Nishiyama KK, Macdonald HM, Buie HR, Hanley DA, Boyd SK. Postmenopausal women with osteopenia have higher cortical porosity and thinner cortices at the distal radius and tibia than women with normal aBMD: an in vivo HR-pQCT study. Journal of Bone and Mineral Research. Apr 2010;25(4):882-90.
75. Kawalilak CE, Johnston JD, Olszynski WP, Kontulainen SA. Characterizing microarchitectural changes at the distal radius and tibia in postmenopausal women using HR-pQCT. Osteoporos Int. Aug 2014;25(8):2057-66.
76. Shanbhogue VV, Brixen K, Hansen S. Age- and Sex-Related Changes in Bone Microarchitecture and Estimated Strength: A Three-Year Prospective Study Using HRpQCT. Journal of bone and mineral research : the official journal of the American Society for Bone and Mineral Research. Aug 2016;31(8):1541-9.
77. Van Ee CA, Chasse AL, Myers BS. Quantifying skeletal muscle properties in cadaveric test specimens: effects of mechanical loading, postmortem time, and freezer storage. Journal of biomechanical engineering. Feb 2000;122(1):9-14.
78. Burt LA, Hanley DA, Boyd SK. Cross-sectional versus longitudinal change in a prospective HR-pQCT study. Journal of Bone and Mineral Research. 2017;32(7):1505-13.
79. Burghardt AJ, Pialat JB, Kazakia GJ, Boutroy S, Engelke K, Patsch JM, et al. Multicenter precision of cortical and trabecular bone quality measures assessed by high-resolution peripheral quantitative computed tomography. Journal of Bone and Mineral Research. Mar 2013;28(3):524-36.
80. Medical S. Scanco Medical Finite Element Software. Version 1.13 ed. Bruetisellen, Switzerland: SCANCO Medical Ag Fabrikweg 2 CH-8306; 2009.
81. Smith M, Bain GI, Turner PC, Watts AC. Review of imaging of scaphoid fractures. ANZ journal of surgery. 2010;80(1-2):82-90.

82. Logan AJ, Lindau TR. The management of distal ulnar fractures in adults: a review of the literature and recommendations for treatment. Strategies in trauma and limb reconstruction. 2008;3(2):49-56.
83. Birkbeck DP, Failla JM, Hoshaw SJ, Fyhrie DP, Schaffler M. The interosseous membrane affects load distribution in the forearm. The Journal of hand surgery. Nov 1997;22(6):975-80.
84. af Ekenstam FW, Palmer AK, Glisson RR. The load on the radius and ulna in different positions of the wrist and forearm. A cadaver study. Acta orthopaedica Scandinavica. Jun 1984;55(3):363-5.
85. Markolf KL, Lamey D, Yang S, Meals R, Hotchkiss R. Radioulnar load-sharing in the forearm. A study in cadavera. J Bone Joint Surg Am. Jun 1998;80(6):879-88.
86. Palmer AK, Werner FW. Biomechanics of the distal radioulnar joint. Clin Orthop Relat Res. Jul-Aug 1984(187):26-35.
87. Shaaban H, Giakas G, Bolton M, Williams R, Wicks P, Scheker LR, et al. The load-bearing characteristics of the forearm: pattern of axial and bending force transmitted through ulna and radius. J Hand Surg Br. Jun 2006;31(3):274-9.
88. Trumble T, Glisson RR, Seaber AV, Urbaniak JR. Forearm force transmission after surgical treatment of distal radioulnar joint disorders. The Journal of hand surgery. Mar 1987;12(2):196-202.
89. Ohman C, Dall'Ara E, Baleani M, Van Sint Jan S, Viceconti M. The effects of embalming using a 4% formalin solution on the compressive mechanical properties of human cortical bone. Clinical Biomechanics. Dec 2008;23(10):1294-8.
90. Burkhart TA, Quenneville CE, Dunning CE, Andrews DM. Development and validation of a distal radius finite element model to simulate impact loading indicative of a forward fall. Proceedings of the Institution of Mechanical Engineers, Part H: Journal of Engineering in Medicine. 2014;228(3):258-71.
91. Keyak J, Rossi S, Jones K, Les C, Skinner H. Prediction of fracture location in the proximal femur using finite element models. Medical engineering & physics. 2001;23(9):657-64.

APPENDIX A: LOAD-DISPLACEMENT CURVES

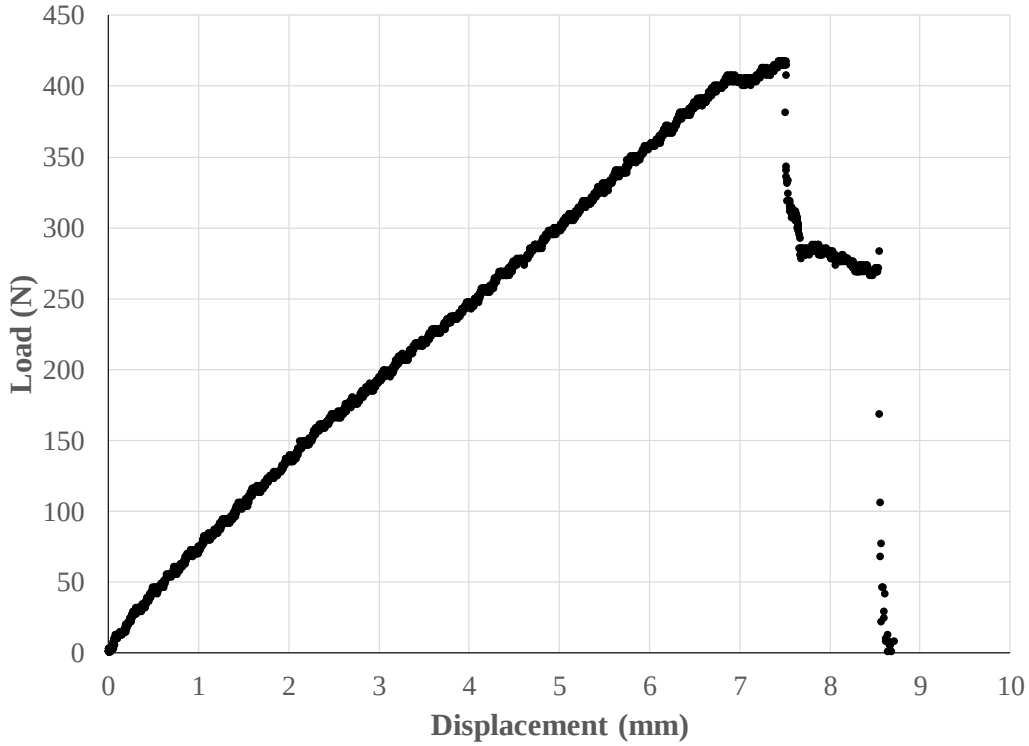

Figure A-1. Load-displacement curve for MT-14-05024R.

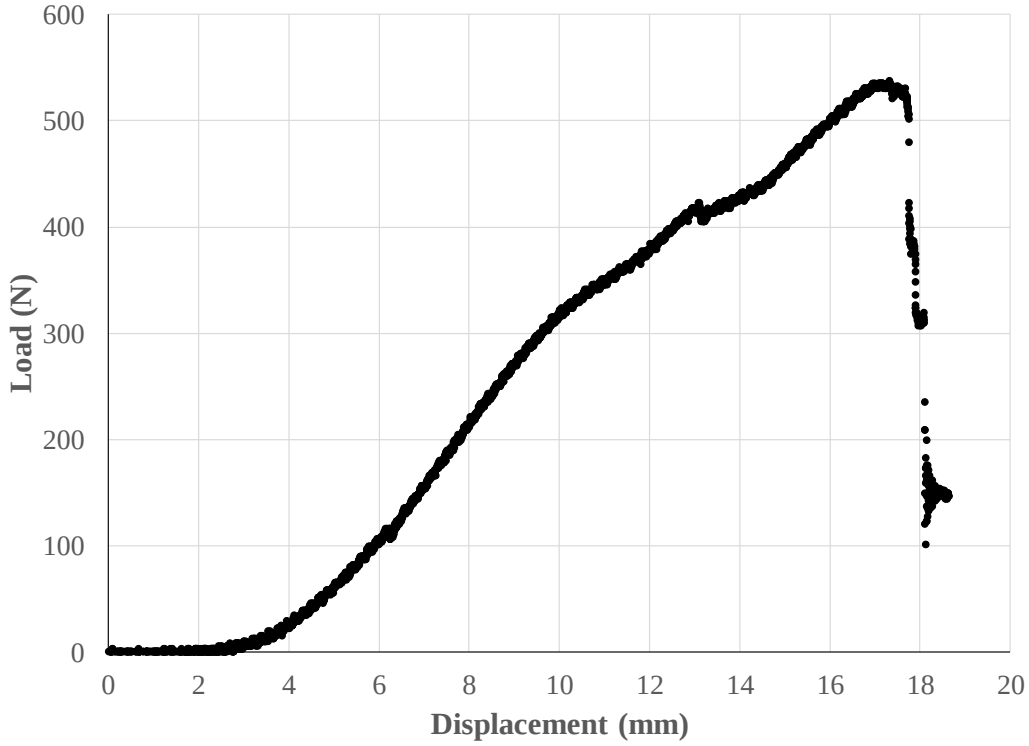

Figure A-2. Load-displacement curve for MT-14-06029L.

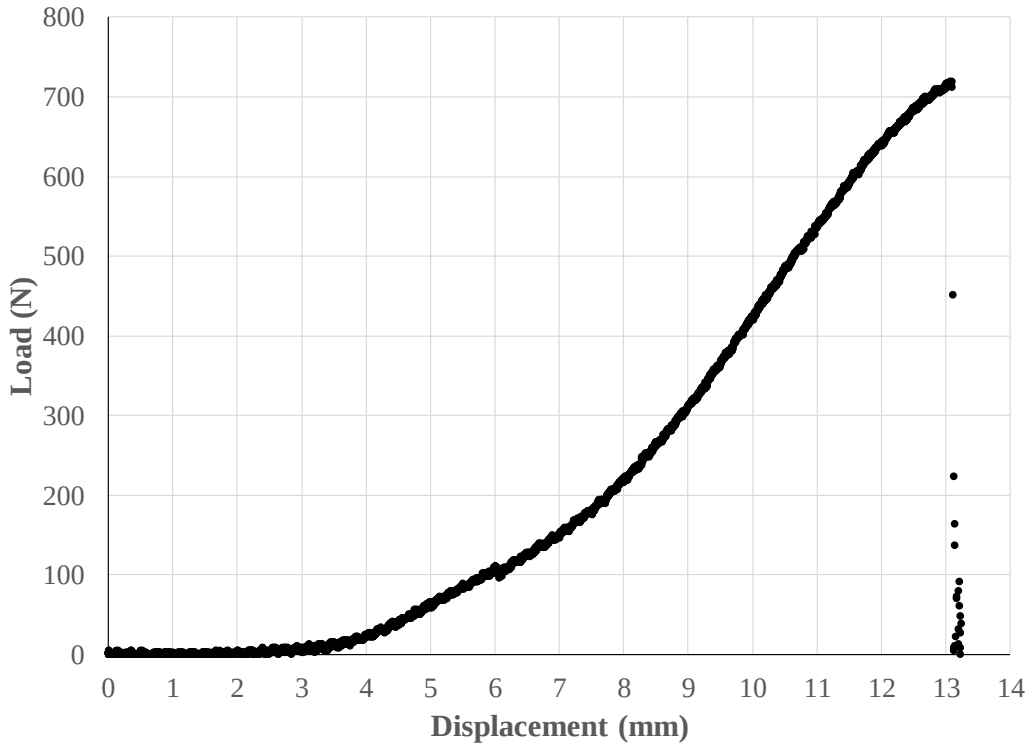

Figure A-3. Load-displacement curve for MT-14-06059L.

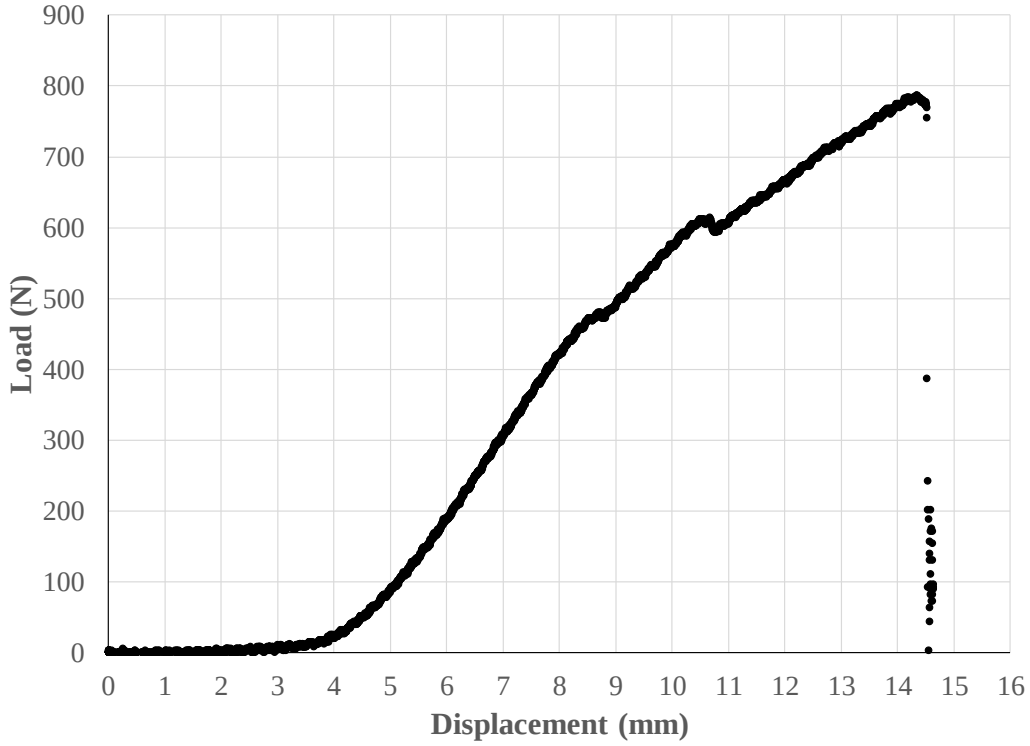

Figure A-4. Load-displacement curve for MT-14-07041L.

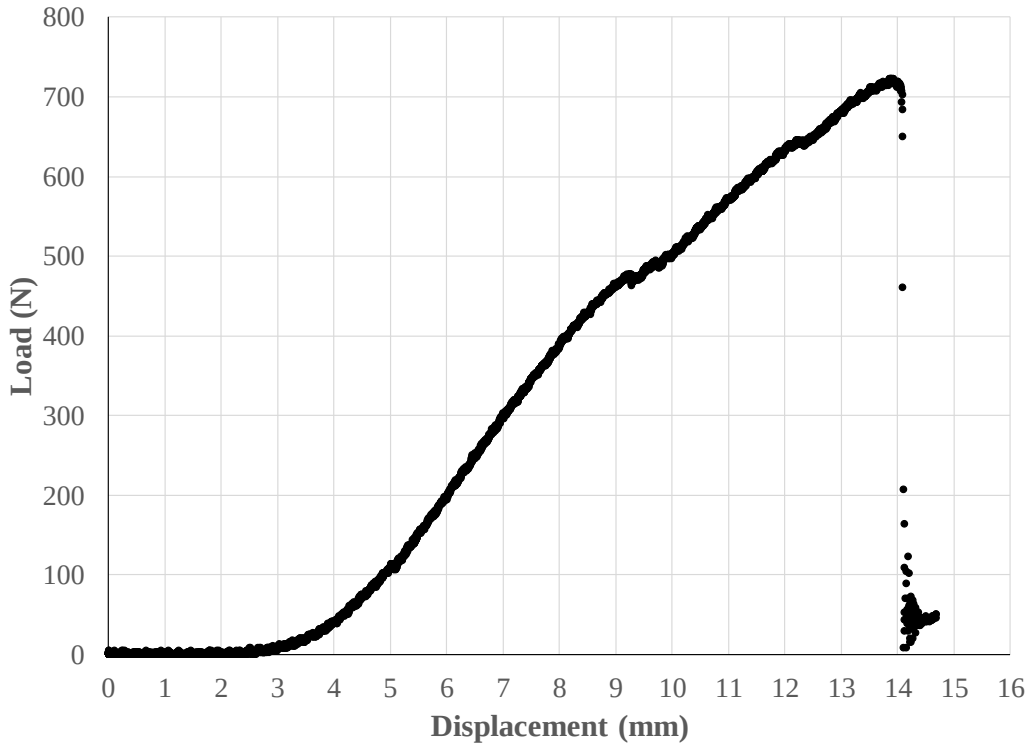

Figure A-5. Load-displacement curve for MT-14-08067R.

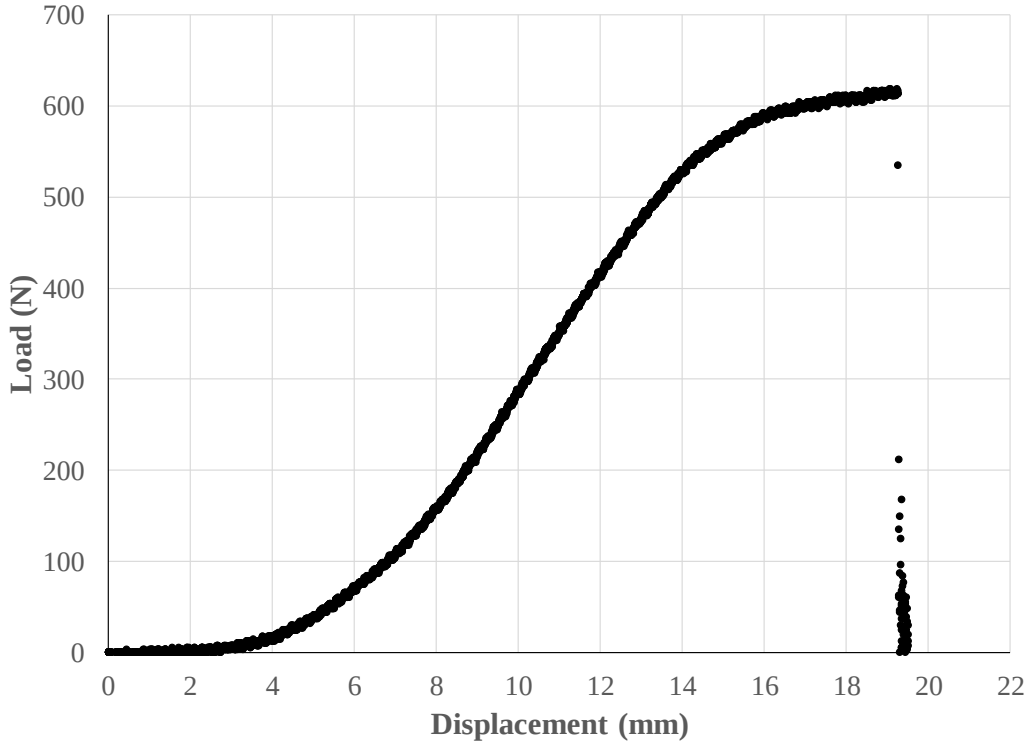

Figure A-6. Load-displacement curve for MT-15-02009L.

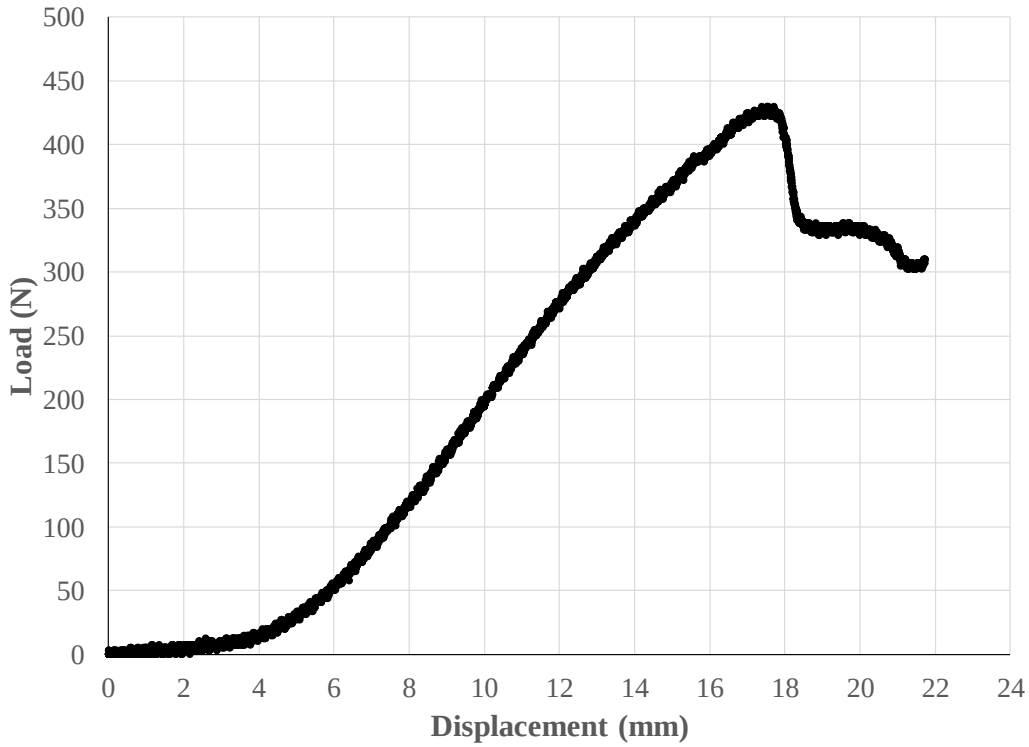

Figure A-7. Load-displacement curve for MT-15-02020R.

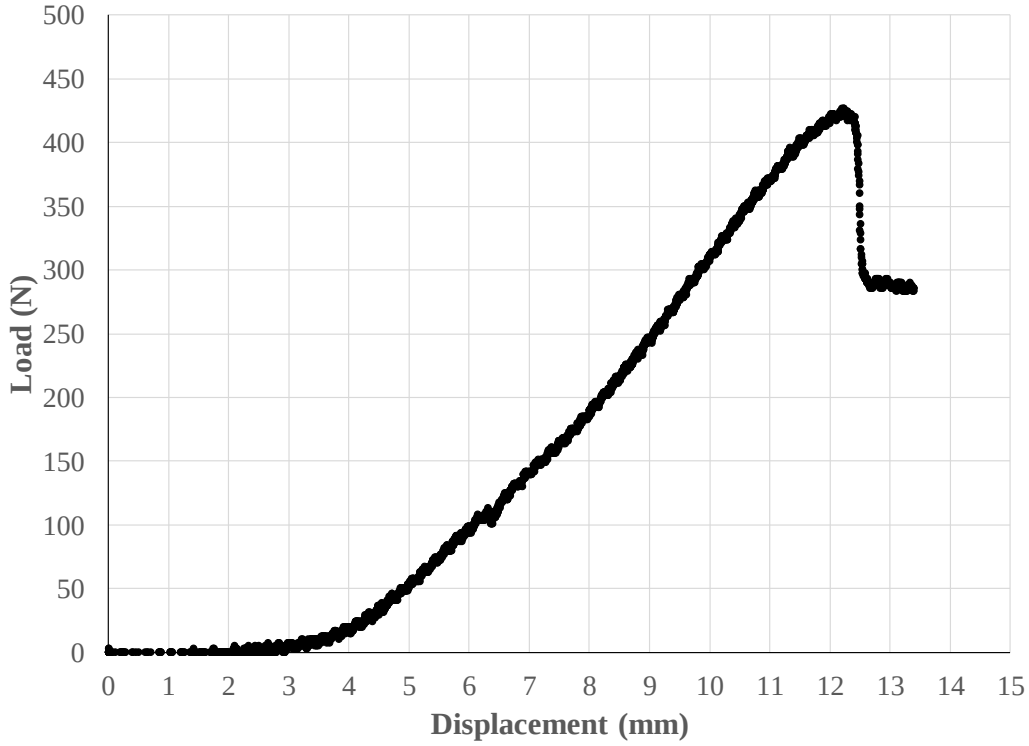

Figure A-8. Load-displacement curve for MT-15-02039L.

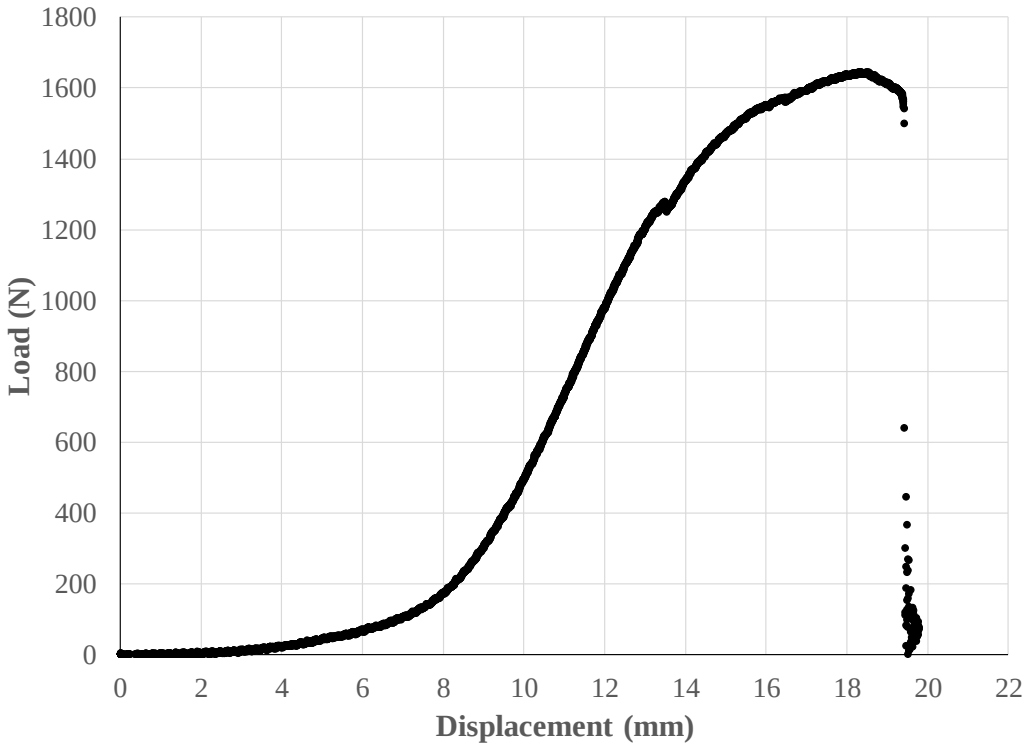

Figure A-9. Load-displacement curve for MT-15-03014R.

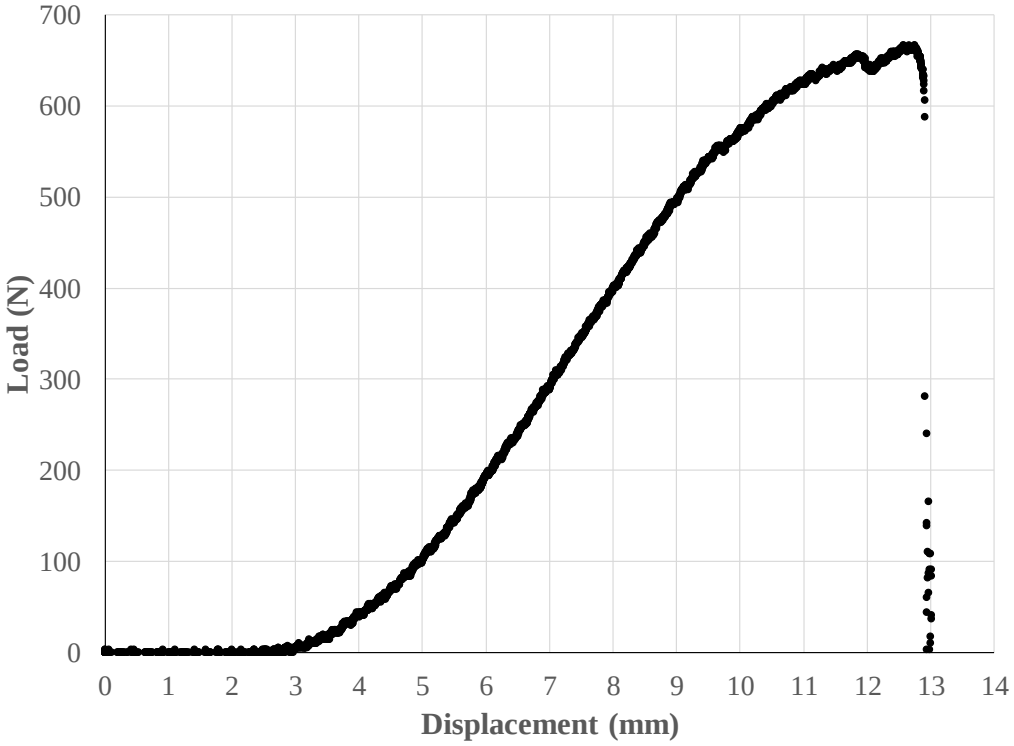

Figure A-10. Load-displacement curve for MT-15-03022R.

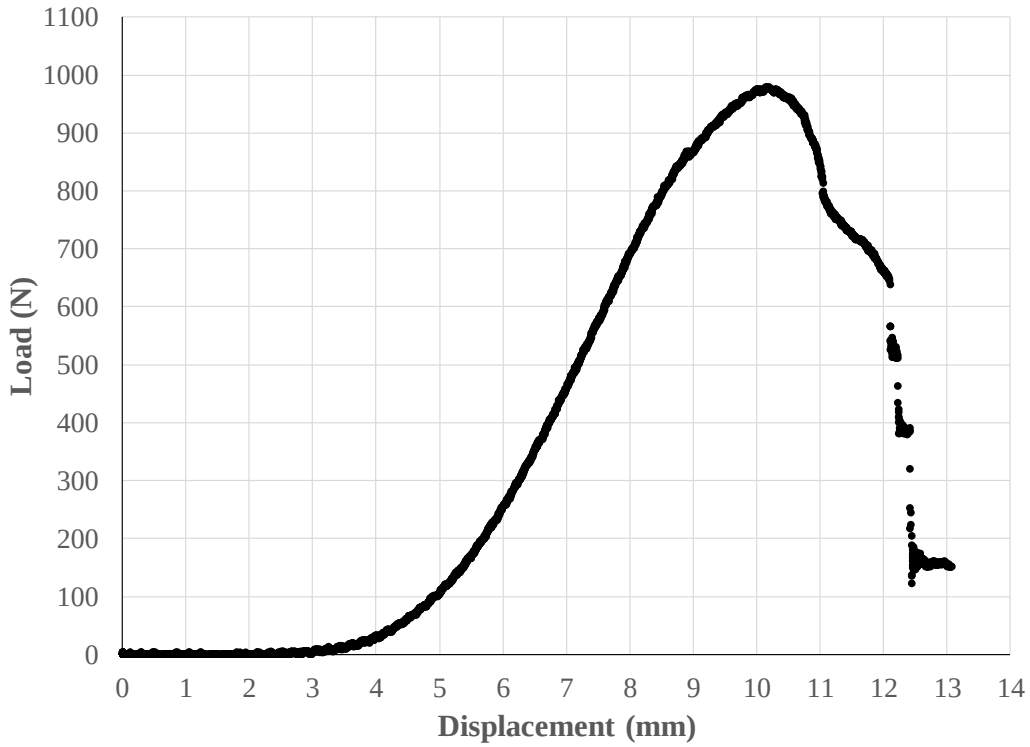

Figure A-11. Load-displacement curve for MT-15-03035R.

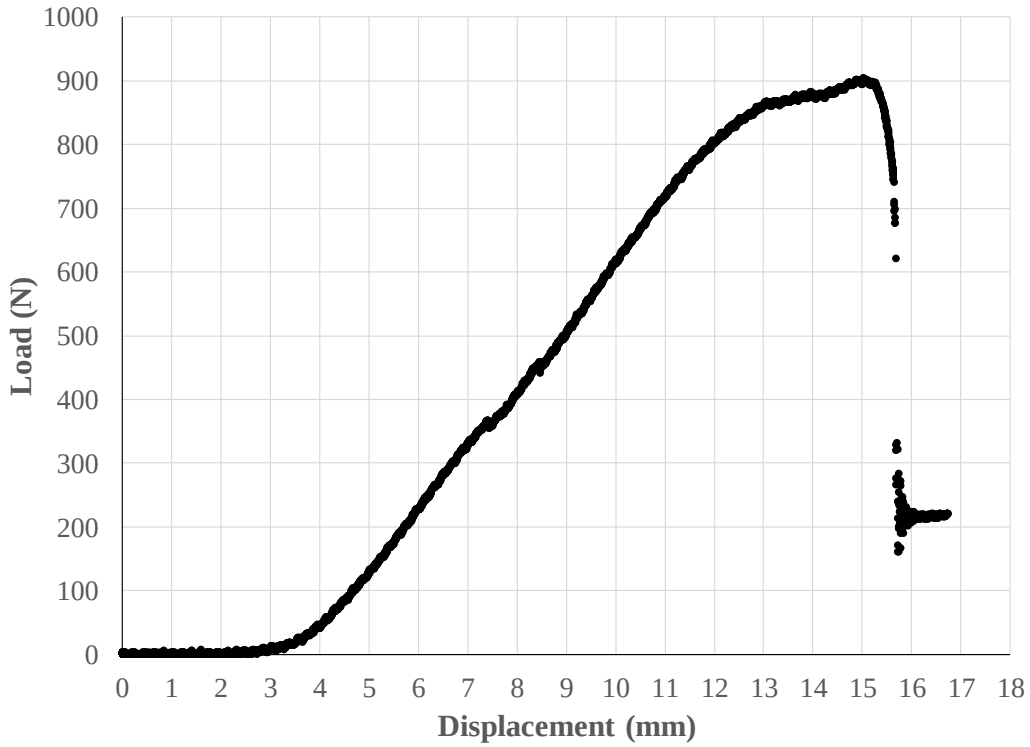

Figure A-12. Load-displacement curve for MT-15-06064R.

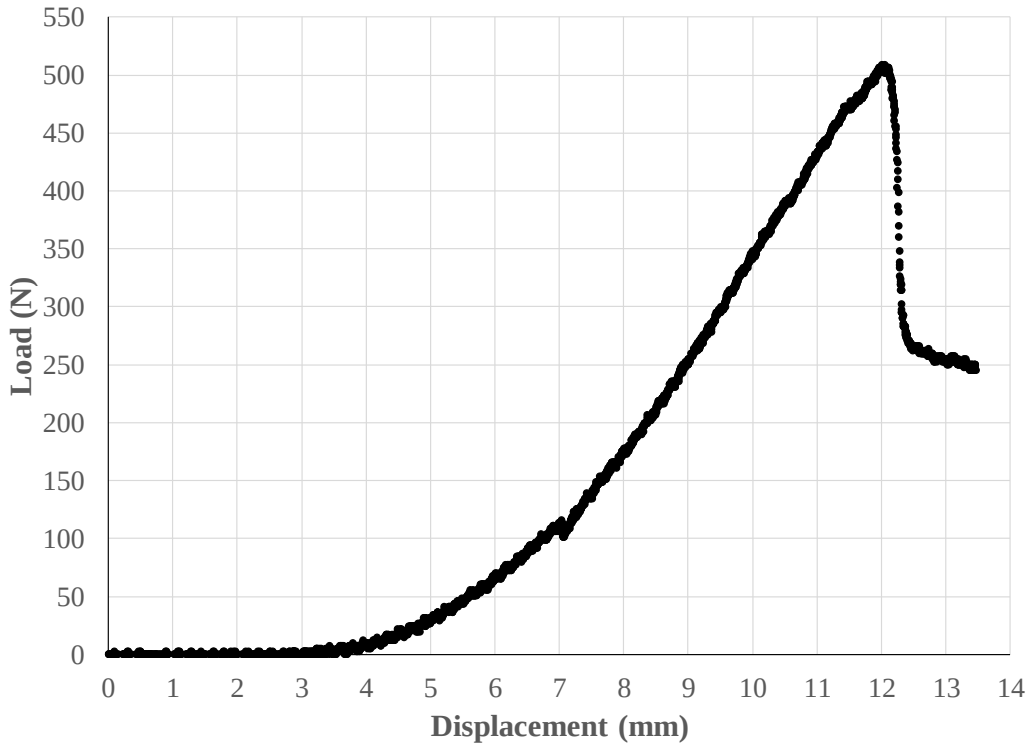

Figure A-13. Load-displacement curve for MT-15-07012R.

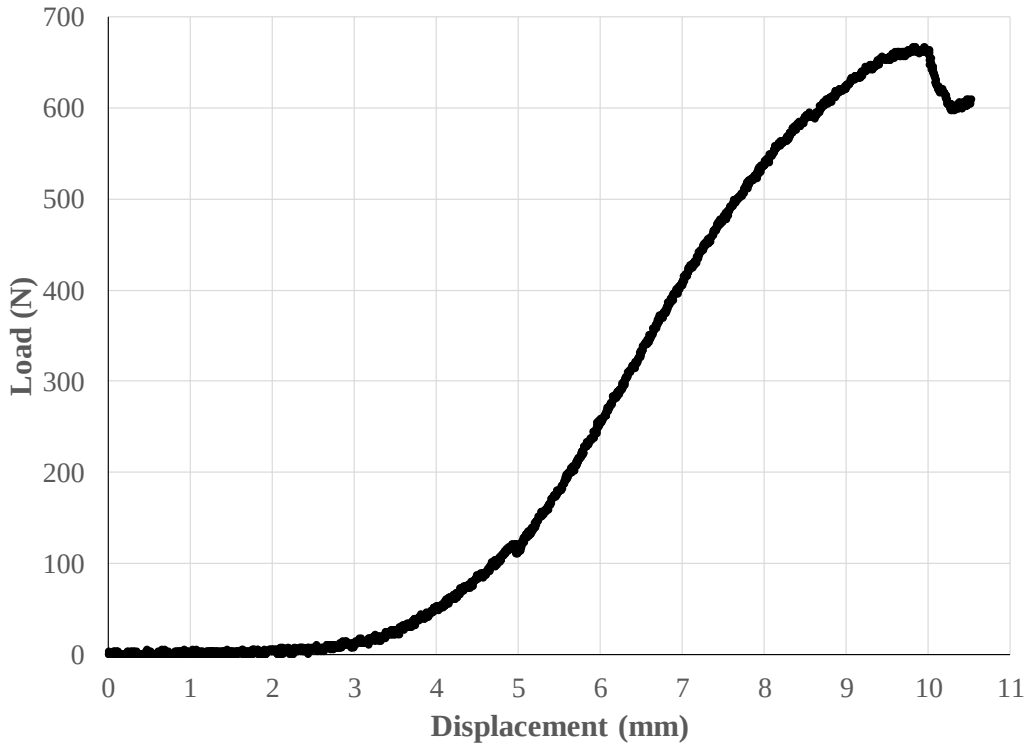

Figure A-14. Load-displacement curve for MT-15-07037R.

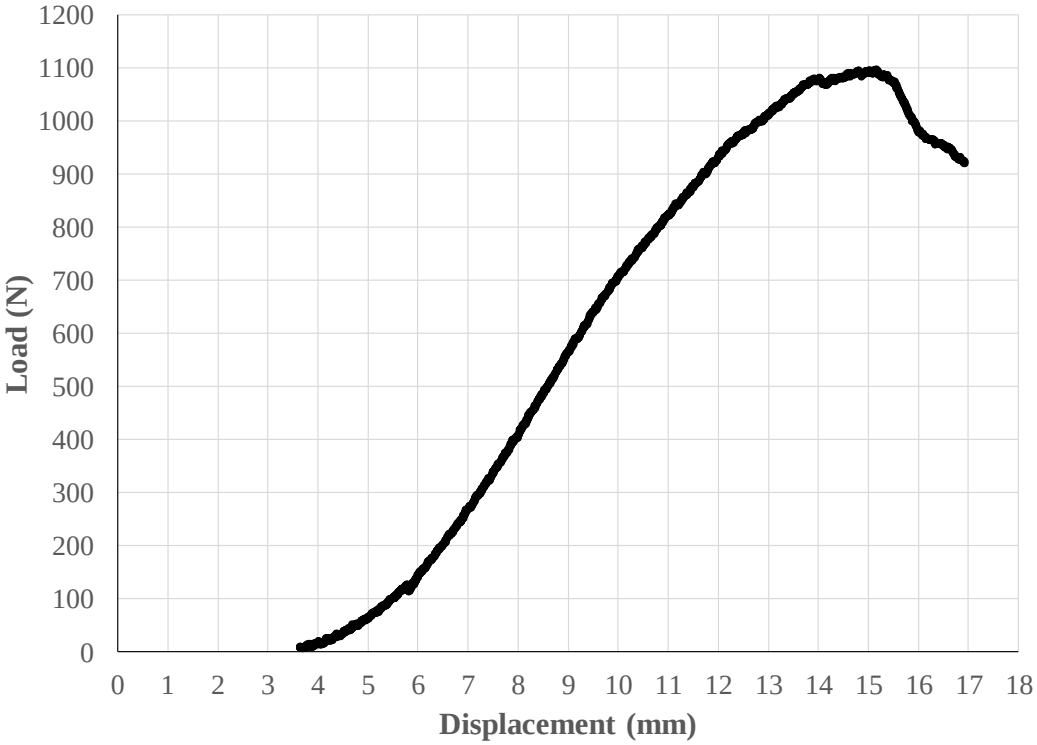

Figure A-15. Load-displacement curve for MT-15-08059R.

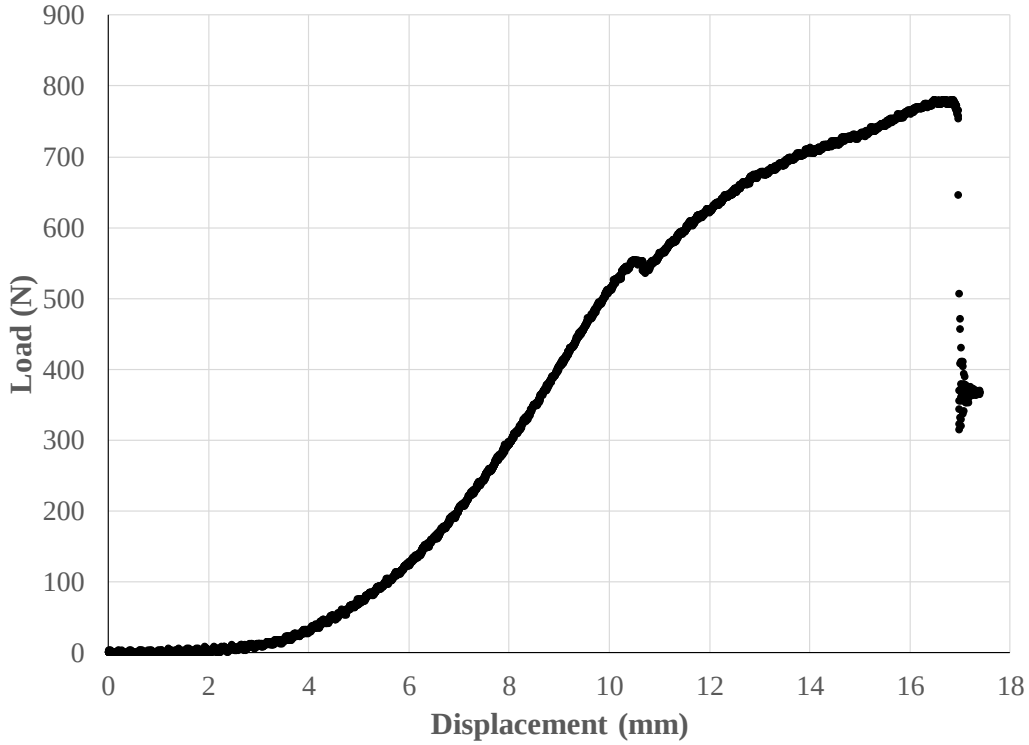

Figure A-16. Load-displacement curve for MT-15-09011R.

APPENDIX B: RESULTS OBTAINED FROM OTHER FAILURE CRITERIA

a) 1 mm Dorsal Offset

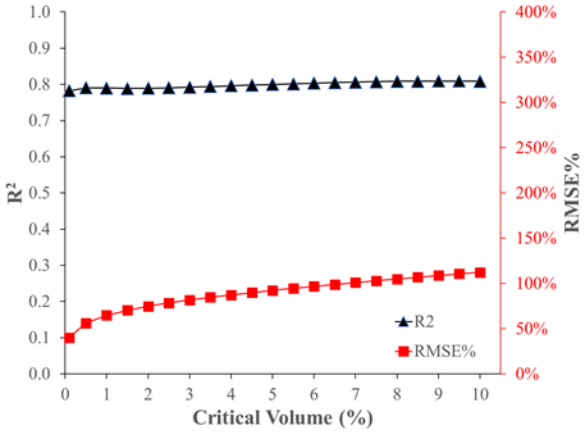

b) Pure Compression

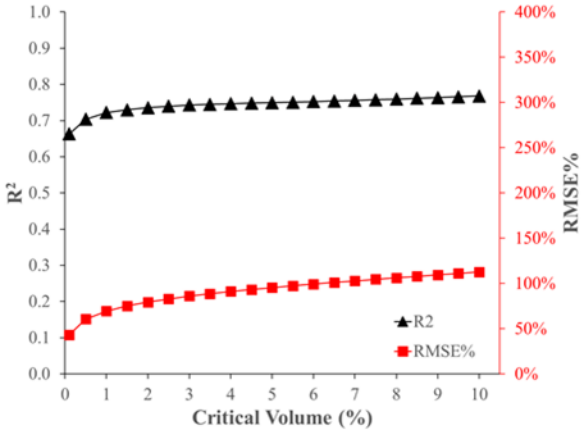

c) (8,7) mm Medial-Dorsal Offset

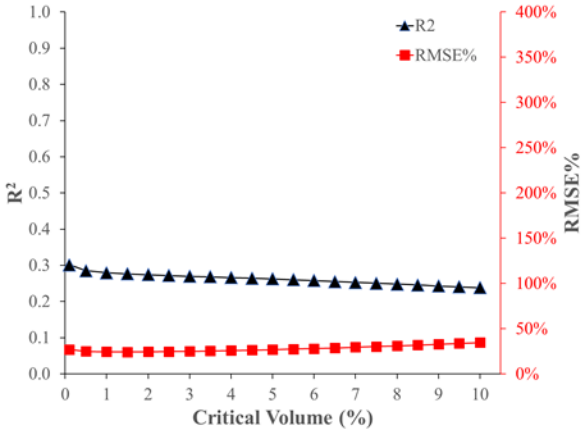

Figure B-1. Energy-Equivalent Effective strain results. Changes in explained variance (R^2; black) and root mean squared error percentage (RMSE%; red) for a percentage based critical volume.

a) 1 mm Dorsal Offset

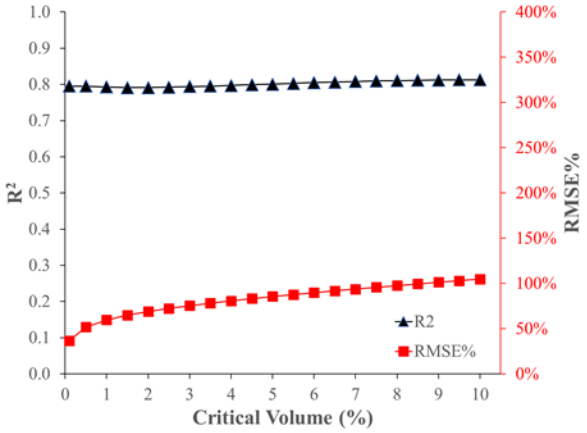

b) Pure Compression

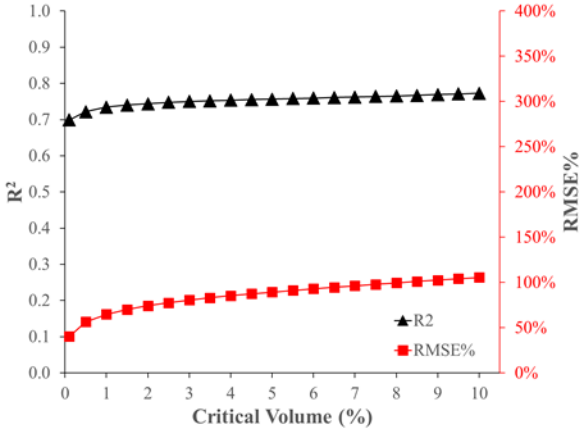

c) (8,7) mm Medial-Dorsal Offset

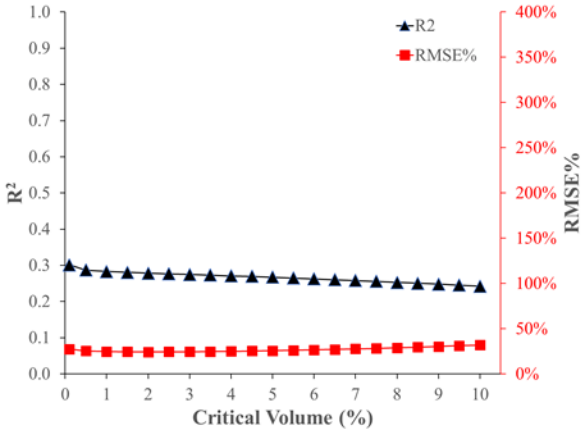

Figure B-2. Hoffman strain results. Changes in explained variance (R^2; black) and root mean squared error percentage (RMSE%; red) for a percentage based critical volume.

a) 1 mm Dorsal Offset

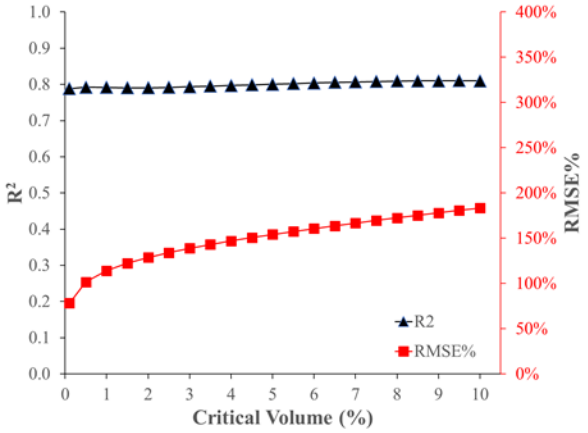

b) Pure Compression

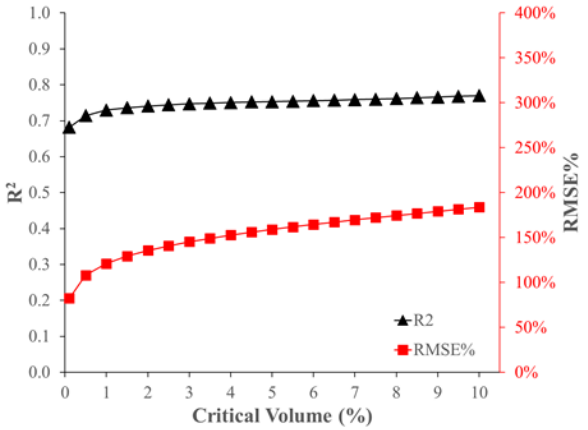

c) (8,7) mm Medial-Dorsal Offset

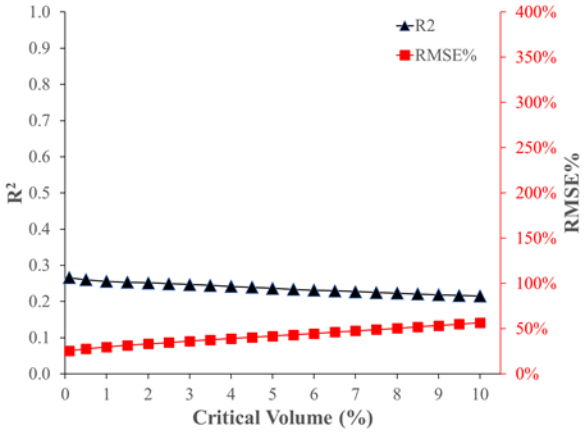

Figure B-3. Maximum principal strain results. Changes in explained variance (R^2; black) and root mean squared error percentage (RMSE%; red) for a percentage based critical volume.